Palaeogeography, Palaeoclimatology, Palaeoecology 661 (2025) 112711

Contents lists available at ScienceDirect

Palaeogeography, Palaeoclimatology, Palaeoecology

journal homepage: www.elsevier.com/locate/palaeo

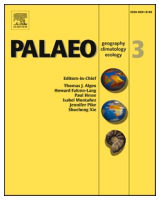

Invited Research Article

# 20,000 days in the life of a giant clam reveal late Miocene tropical climate variability

Iris Arndt [a,b,*], Miguel Bernecker [a], Tobias Erhardt [a,b], David Evans [b,c], Jens Fiebig [a], Maximilian Fursman [a,b], Jorit Kniest [a,b,1], Willem Renema [d,e], Vanessa Schlidt [a,b], Philip Staudigel [a], Silke Voigt [a,b], Wolfgang Müller [a,b]

[a] Institute of Geosciences, Goethe University Frankfurt, Frankfurt am Main, Germany
[b] Frankfurt Isotope and Element Research Center (FIERCE), Goethe University Frankfurt, Frankfurt am Main, Germany
[c] School of Ocean and Earth Science, University of Southampton, Southampton, United Kingdom
[d] Marine Biodiversity Group, Naturalis Biodiversity Center, Leiden, the Netherlands
[e] Institute for Biodiversity and Ecosystem Dynamics (IBED), University of Amsterdam, Amsterdam, the Netherlands

ARTICLE INFO

Editor: M Elliot

*Keywords:*
Elemental ratio analysis via LA-ICPMS
Sub-daily resolution
Internal age model
(Sub-seasonal) palaeoclimate reconstruction
ENSO
Dual clumped isotopes

ABSTRACT

Giant clams (*Tridacna*) are well-suited archives for studying past climates at (sub-)seasonal timescales, even in 'deep-time' due to their high preservation potential. They are fast growing (mm-cm/year), live several decades and build large aragonitic shells with seasonal to daily growth increments. Here we present a multi-proxy record of a late Miocene *Tridacna* that grew on the western margin of the Makassar Strait (Indonesia). By analysing daily elemental cycle lengths using our recently developed Python script Daydacna, we build an internal age model, which indicates that our record spans 20,916 ± 1220 days (2 SD), i.e. ~57 ± 3 years. Our temporally resolved dataset of elemental ratios (El/Ca at sub-daily resolution) and stable oxygen and carbon isotopes ($\delta^{18}O$ and $\delta^{13}C$ at seasonal to weekly resolution) was complemented by dual clumped isotope measurements, which reveal that the shell grew in isotopic equilibrium with seawater. The corresponding $\Delta_{47}$ value yields a temperature of 27.9 ± 2.4 °C (2 SE) from which we calculate a mean oxygen isotopic composition of late Miocene tropical seawater of −0.43 ± 0.50 ‰. In our multi-decadal high temporal resolution records, we found multi-annual, seasonal and daily cycles as well as multi-day extreme weather events. We hypothesise that the multi-annual cycles (slightly above three years) might reflect global climate phenomena like ENSO, with the more clearly preserved yearly cycles indicating regional changes of water inflow into the reef, which together impact the local isotopic composition of water, temperature and nutrient availability. In addition, our chronology indicates that twice a year a rainy and cloudy season, presumably related to the passing of the ITCZ, affected light availability and primary productivity in the reef, reflected in decreased shell growth rates. Finally, we find irregularly occurring extreme weather events likely connected to heavy precipitation events that led to increased runoff, high turbidity, and possibly reduced temperatures in the reef.

## 1. Introduction

Bivalve shells are important archives of (palaeo)climate and environmental changes and can provide continuous decadal records at very high (seasonal to sub-daily) time resolution (e.g. Ayling et al., 2015; Batenburg et al., 2011; de Winter et al., 2020b; Elliot et al., 2009; Hori et al., 2015; Nützel et al., 2010; Peharda et al., 2021; Schöne et al., 2011; Shao et al., 2020; Warter and Müller, 2017; Watanabe et al., 2004). Their dense structure makes them less sensitive to diagenetic recrystallisation compared to other high time-resolution environmental archives such as corals, which is especially relevant for 'deep-time', i.e. pre-Pleistocene, palaeoenvironmental reconstructions (Griffiths et al., 2013; Veeh and Chappell, 1970; Welsh et al., 2011). 'Deep-time' temperature seasonality has been studied using the oxygen isotopic ($\delta^{18}O$) compositions of bivalve shells, e.g. for the Cretaceous (Steuber et al., 2005; Walliser et al., 2018), Triassic (Nützel et al., 2010) or Permian

* Corresponding author at: Institute of Geosciences, Goethe University Frankfurt, Altenhöferallee 1, 60438 Frankfurt am Main, Germany.
*E-mail address:* arndt@em.uni-frankfurt.de (I. Arndt).
[1] Current address: GEOMAR Helmholtz Centre for Ocean Research Kiel, Kiel, Germany.

https://doi.org/10.1016/j.palaeo.2024.112711
Received 30 June 2024; Received in revised form 29 October 2024; Accepted 30 December 2024
Available online 2 January 2025
0031-0182/© 2025 The Authors. Published by Elsevier B.V. This is an open access article under the CC BY license (http://creativecommons.org/licenses/by/4.0/).

(Ivany and Runnegar, 2010) alongside other archives and proxies (e.g. Evans et al., 2013; Ivany and Judd, 2022). (Sub-)daily environmental changes in the past have been revealed through element ratios e.g. for the Neogene (Sano et al., 2012; Warter and Müller, 2017), or the Cretaceous (de Winter et al., 2020b). Environmental parameters which have been reconstructed sub-seasonally from bivalve shells include temperature (e.g., Ayling et al., 2015; Batenburg et al., 2011; Pätzold et al., 1991; Warter et al., 2015), nutrient availability (Arias-Ruiz et al., 2017; Batenburg et al., 2011; Elliot et al., 2009), irradiance and diurnal cycle lengths (de Winter et al., 2020a; Hori et al., 2015; Sano et al., 2012; Warter et al., 2018) and short-term disturbances such as past extreme weather events including storms and heavy precipitation events (Komagoe et al., 2018; Yan, 2020).

(Sub)tropical marine giant clams (*Tridacna)* are long-lived, fast-growing organisms (mm-cm/year, e.g. Arndt et al., 2023; Bonham, 1965; Elliot et al., 2009; Fousiya et al., 2024; Ma et al., 2020; Mills et al., 2023; Rosewater, 1965) that can build large aragonitic shells of up to one meter in size over some hundred years (Knop, 1996; Watanabe et al., 2004). Therefore, their shells are ideally suited to record multi-decadal environmental changes at sub-seasonal resolution in (sub-)tropical reefs, ever since their emergence in the early Miocene (Harzhauser et al., 2008).

The late Miocene (~10 Ma; see below) *Tridacna* specimen investigated in this study was collected in East Kalimantan. It grew on the western margin of the Makassar Strait, a key part of the Indonesian Throughflow (ITF), which affects global atmospheric climate patterns (e.g., Gallagher et al., 2024; Schneider, 1998). The late Miocene was characterised by $pCO_2$ values of ~400–500 ppm (Rae et al., 2021) with global mean surface temperatures ~3–4 °C higher than modern (Evans et al., 2024; LaRiviere et al., 2012; Pound et al., 2011; Zhang et al., 2014). A considerable reduction in atmospheric $CO_2$ (Rae et al., 2021) combined with eccentricity minima facilitated the growth and stabilisation of the Antarctic ice sheet during the Mid-Miocene Climate Transition (MMCT) at ~14.5 to 13 Ma (Holbourn et al., 2005), resulting in a sea level decrease of ~50 m (John et al., 2011). These changes in sea level and the tectonic closure of the Indonesian ocean gateway in the late Oligocene/early Miocene (Kuhnt et al., 2004) influenced the formation and position of the proto-West Pacific Warm Pool. The formation of the earliest proto-West Pacific Warm Pool in the late Miocene is thought to have induced an ocean-atmospheric pattern similar to today with variable Walker circulation strength, a La Niña main state and El Niño-Southern Oscillation (ENSO)-like dynamics (Fox et al., 2021; Gallagher et al., 2024; Sosdian and Lear, 2020). The cooling of the Southern Ocean in the late Miocene led to a northward shift of the intertropical convergence zone (ITCZ) in the austral summer (Holbourn et al., 2010), from an equator-near position at 15 Ma to ~10° N at 8 Ma (Groeneveld et al., 2017). Additionally, a combination of tectonic changes, such as the closure of the Tethys and the uplift of the Himalayan Plateau, reorganised ocean circulation and induced global cooling which intensified the South Asian Monsoon at ~13 Ma (Betzler et al., 2018 and refs. therein).

Because of these changes in ocean circulation and precipitation patterns, the Miocene is a particularly interesting epoch to study in the Indo-Pacific region. Through dual clumped isotope analysis (Fiebig et al., 2019), we determine that the giant clam shell was precipitated indistinguishably from isotopic equilibrium and gain a temperature as well as a seawater $\delta^{18}O$ value for this late Miocene Indo-Pacific reef. Based on elemental ratios and stable isotopic composition, we present a 57-year long continuous multiproxy palaeoenvironmental record to provide multidecadal information at up to daily time-resolution, revealing multi-annual ENSO-like cycles, regional precipitation driven seasonal patterns and extreme weather events during the Miocene. Such (sub-)seasonal data help to constrain palaeoclimate reconstructions and can further be utilized to test the skill of climate models (Carré and Cheddadi, 2017; Cauquoin et al., 2019; Schmidt et al., 2014; Tierney et al., 2020).

## 2. Materials

A large *Tridacna* shell, referred to as TOBI (Fig. 1), was collected in 2013 in East Borneo, near Bontang (0°08′15"N, 117°26′21″E). The shell was taken from a bioclastic packstone horizon within silty shales and in close vicinity to a sandstone horizon (Renema et al., 2015).

Following external cleaning with a brush and tap water, the shell was cut along the presumed maximum growth axis (Fig. 1 B). The resultant slab was divided into six smaller rectangular slabs (~3 × 6 cm), each of which in turn was sliced longitudinally. The mirror sides of each of these halves were used to create powder for stable isotope analysis by micromilling and thin sections (50 μm thick) used for laser ablation inductively coupled plasma mass spectrometry (LA-ICPMS) analysis, respectively. The thin sections were polished using a 3 μm diamond suspension.

## 3. Methods

### 3.1. MC-ICPMS – Strontium isotopes

The strontium isotopic composition of the shell was analysed using multi collector inductively coupled plasma mass spectrometry (MC-ICPMS) in solution mode. For the purpose of Strontium Isotope Stratigraphy (SIS), twelve powder samples (10 to 20 mg) were taken using a handheld drill with a diamond tipped drill bit; four samples were selected from optically pristine areas, four from the visibly altered rim areas and four from recrystallised areas. The powder samples were pre-leached for one hour in 0.1 M acetic acid. Subsequently, each sample was centrifuged and the remaining solid phase was leached in 1 M acetic acid at room temperature for another 17 h. For seasonally-resolved Sr isotope data another set of twelve powder samples of 1 to 2 mg were taken from the pristine inner part of the shell using a micromill equipped with a conical, diamond coated drill bit (tip diameter: 0.3 mm). Six samples were taken from areas with dark banding and six from the light areas in between the bands (Fig. 2). The samples were leached in 0.1 M acetic acid for one hour and subsequently centrifuged. The acetic acid leachates of all samples were dried and re-dissolved in 3 M nitric acid before chromatographic Sr purification using the Sr resin SR B50 S with 50–100 μm grain size. These Sr eluates were measured using a Thermo Fisher Neptune Plus MC-ICPMS, equipped with an auto-sampler. The samples were introduced into the plasma using a nebuliser and conventional glass spray chamber. Masses ($m/z$) from 83 to 88, including Kr and Rb interferences, were simultaneously monitored and mass bias was corrected using the exponential mass fractionation law (Russell et al., 1978) and $^{86}Sr/^{88}Sr = 0.1194$ (Steiger and Jäger, 1977), after subtraction of on-peak baselines. NIST SRM987 was used as standard reference material and for tuning. Using a 100 ppb SRM987 solution and a $CeO^+/Ce^+$ rate of 2 %, we achieved an $^{88}Sr$ sensitivity of ~13 V. For SIS analysis, the corresponding SRM987 analyses yielded $^{87}Sr/^{86}Sr$ of 0.710241 ± 0.000007 (2 SD, $n = 10$; $^{88}Sr$ signal ~40 V at $10^{11}$ Ω), and consequently no adjustment to the internationally adopted $^{87}Sr/^{86}Sr$ of 0.710248 (McArthur et al., 2001) was necessary. Material from both leaches were used for SIS analysis, excluding four (of twenty-four) measurements for which we did not obtain sufficiently high $^{88}Sr$ signals. In contrast, during later analysis of seasonally-resolved Sr isotope data, the SRM987 analyses yielded $^{87}Sr/^{86}Sr$ of 0.710283 ± 0.000026 (2 SD, $n = 16$; $^{88}Sr$ signal ~11 V at $10^{11}$ Ω); as a result, the $^{87}Sr/^{86}Sr$ ratios of these samples were adjusted by subtracting 0.000035. Final $^{87}Sr/^{86}Sr$ uncertainties listed in tables S1 and S2 include the quadratically propagated individual internal errors (2 SE) and external SRM987 reproducibilities (2 SD).

### 3.2. LA-ICPMS – Elemental ratios

The thin sections were precleaned in an ultrasonic bath with ethanol. Sub-daily resolved LA-ICPMS data were measured with a RESOlution LR

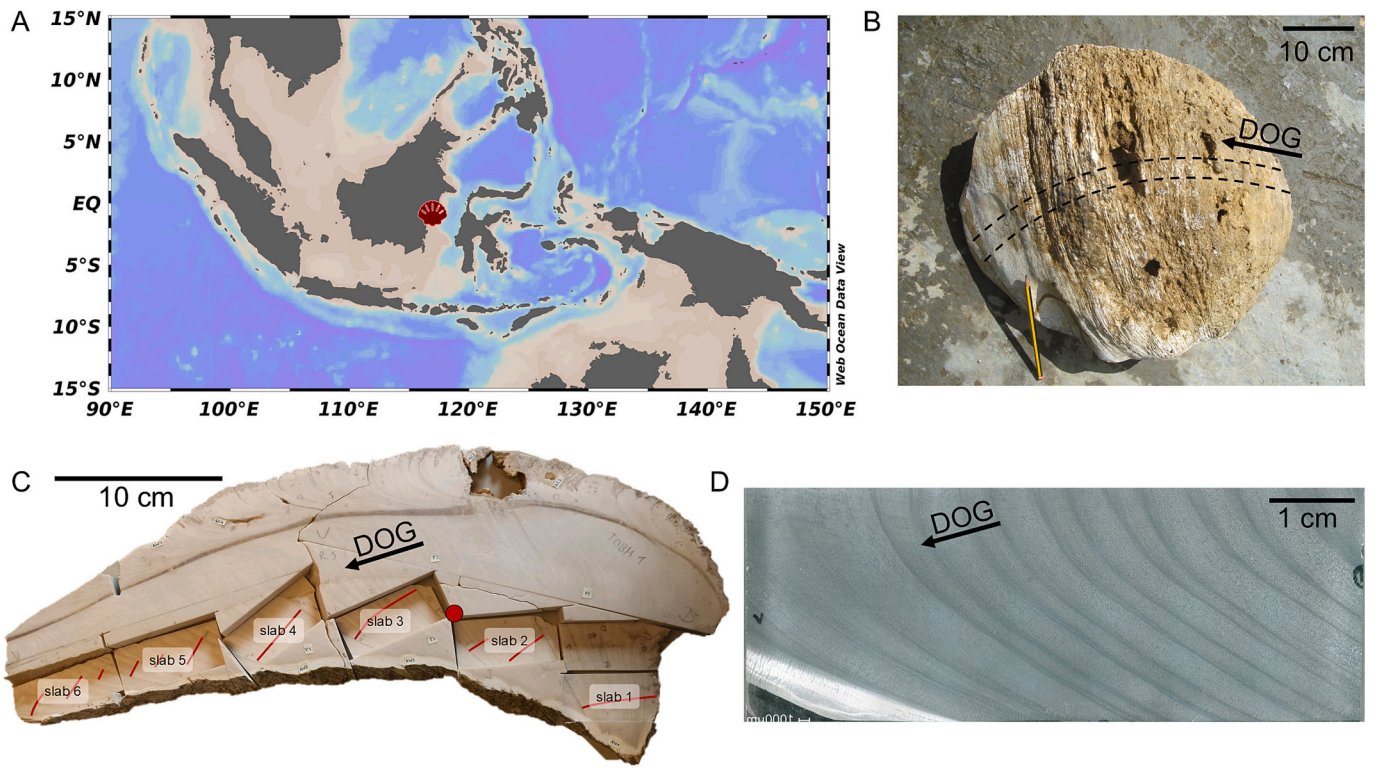


**Fig. 1.** A: Map of the Indo-Pacific region, with the sampling locality (0°08′15″N 117°26′21″E) marked by a red clam icon. B: Sample before cutting, the cutting direction is indicated by the dashed line. C: Section across the shell with numbered cut slabs and red tracks indicating the sampling axis for the geochemical data. The red dot indicates the location of the sample taken for dual clumped analysis. D: Thin section (50 μm thick) of slab 6 with a conspicuously regular double-banding pattern at the 5 to 10 mm scale and visible alteration at the outer rim (lower left corner). The direction of growth (DOG) is from right to left for B, C and D. (For interpretation of the references to colour in this figure legend, the reader is referred to the web version of this article.)

laser-ablation system (Applied Spectra Inc., USA) equipped with a two-volume S155 cell (Laurin Technic; Müller et al., 2009) coupled to a Thermo Fisher Element XR sector field mass spectrometer. We used a 3 × 33 μm rotatable rectangular slit for ablation to maximise spatial resolution while maintaining suitable sensitivity, following Warter and Müller (2017). Pathways were set parallel to the maximum growth axis and orthogonal to the daily bands. Laser precleaning was performed at a scan speed of 7 μm/s and a repetition rate of 20 Hz (using the same laser spot size), while measurements were conducted at 1 μm/s and 10 Hz respectively. The isotopes $^{11}$B, $^{23}$Na, $^{24}$Mg, $^{27}$Al, $^{43}$Ca, $^{89}$Y, $^{88}$Sr, $^{138}$Ba were monitored with a sweep time of 330 ms to achieve a sampling interval of ~0.34 μm (distance per sweep time). Instrumental tuning was performed on standard reference material NIST SRM612 with a 60 μm spot at 1 μm/s scan speed and 5 Hz repetition rate, tuning the plasma to minimise the oxide production rate to ≤0.4 % for $ThO^+/Th^+$, to achieve a Th/U ratio of 0.97 and normalised argon index (Fietzke and Frische, 2016) of 1.1. The doubly-charged production rate was monitored via the 22/44 ratio and was ~1.5 %.

Sample measurements were bracketed with NIST SRM612 as external standard, analysed in an identical manner as the samples, with all reference values taken from Jochum et al. (2011) with the exception of Mg, for which we follow the recommendation of Evans and Müller (2018). The Ca concentration of the shell was assumed to be 40 wt% based on aragonite stoichiometry (but not required for El/Ca). Elemental ratio (El/Ca) quantification was conducted after Longerich et al. (1996) using the software Iolite 4 (Paton et al., 2011) with $^{43}$Ca as internal standard. Accuracy and precision were determined by measuring the MPI-DING glass KL2-G (Jochum et al., 2006) and the nanopellet carbonate standard MACS-3NP (Garbe-Schönberg and Müller, 2014). Accuracies are in the range of −2 to 5 % for KL2-G and 7 to 32 % for MACS-3NP, while precision ranged from 2 to 14 % 2 RSD for KL2-G and 3 to 18 % 2 RSD for MACS-3NP; for full details see table S3. Data processing and visualisation was conducted via Python and benefited from the Python libraries and packages NumPy (Harris et al., 2020), Pandas (Reback et al., 2022), Matplotlib (Caswell et al., 2022) and PyCWT, based on Torrence and Compo (1998). For details, see Arndt et al. (2023).

### 3.3. Gas MS – Stable oxygen and carbon isotopes

Powder samples of ~100 μg each were taken from the shell slabs using a NewWave micromill along the entire shell length at increments of 100–200 μm for the ontogenetically younger slabs (slabs 1–4) and at 300 μm for the ontogenetically older slabs (slabs 5–6), using a conical diamond coated drill bit with a 300 μm tip. First, the outermost rims of the sample path area were drilled, and the powder removed. Then the subsequent samples were removed "quarry-like" in steps below the drill bit's width. The sampling depth was 200 μm in the z-direction and the path length was between 500 and 1000 μm (x-y-direction). The drill bit rotation was reduced to 70 % of maximum drill speed to reduce heating and minimise recrystallisation to calcite while drilling (Moon et al., 2021; Staudigel and Swart, 2016; Waite and Swart, 2015). Approximately 100 μg of sample powder was weighed and inserted into glass exetainers. Samples were loaded into a Gas Bench II (Thermo Fisher) connected to a MAT 253 gas source mass spectrometer (Thermo Fisher) and analysed for their bulk carbon and oxygen isotope compositions. For data correction (Spötl and Vennemann, 2003), an inhouse Carrara marble standard with known isotopic composition was run along with the samples. Final $\delta^{13}$C and $\delta^{18}$O values are reported relative to VPDB.

### 3.4. Gas MS – Dual clumped isotopes

A block was cut from the inner shell part, ground with an agate mortar and sieved through a 100 μm mesh. $\Delta_{47}$, $\Delta_{48}$, $\delta^{18}$O and $\delta^{13}$C of

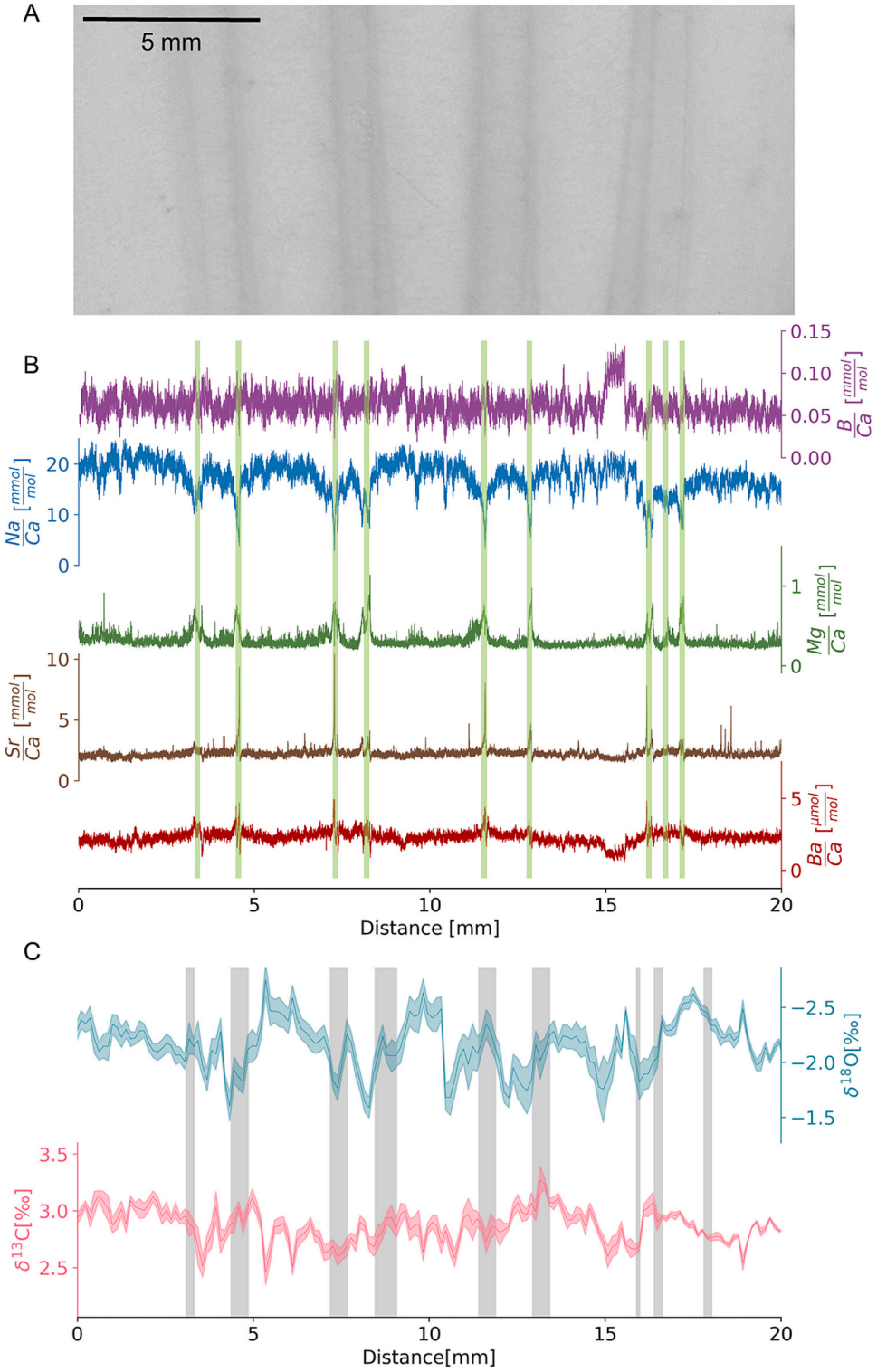


**Fig. 2.** A: Image of the shell showing the optically visible light-dark banding pattern. B: Corresponding El/Ca data from the shell section shown in A, which demonstrate the covariation of the elemental ratio variability with the growth banding. Note that the positions of the green bars in panel B are defined on the basis of the Mg/Ca and Na/Ca peaks (see Arndt et al., 2023, Fig. S16) and not directly determined by the position of the shell's dark bands. C: Stable oxygen and carbon data from the shell section, with optically determined dark bands (as in A) shown in grey. Unlike El/Ca ratios (Mg/Ca, Na/Ca), no direct correlation between the dark shell bands (in grey) and the isotopic composition is observed. (For interpretation of the references to colour in this figure legend, the reader is referred to the web version of this article.)

this sample were measured on a Thermo Scientific 253 Plus gas source mass spectrometer using the setup and following the methodology of Fiebig et al. (2019, 2021) and Bernecker et al. (2023). Acid digestion was conducted with phosphoric acid (>108 wt%) at 90 °C on 8 replicates. For each replicate, 10.0 ± 0.2 mg of the fine powder was weighed into a silver capsule. Alongside the samples we measured carbonate standards ETH-1 and ETH-2 (Bernasconi et al., 2021), Carrara marble, GU1, as well as $CO_2$ gases of varying bulk isotopic compositions

equilibrated at 25 °C and 1000 °C. All samples and secondary standards were measured against a reference gas with known isotopic compositions of $\delta^{13}C_{VPDB} = -4.2$ ‰ and $\delta^{18}O_{VSMOW} = 25.26$ ‰ (ISO-TOP, Air Liquide, France). Raw intensity data were corrected for the pressure baseline effect utilizing a *m/z* 47.5 half-mass cup and optimised scaling factors (Bernecker et al., 2023; Fiebig et al., 2021), such that equilibrated gases displayed slopes of zero in $\delta^{47}$ vs $\Delta_{47}$ and $\delta^{48}$ vs $\Delta_{48}$ space. Standardisation was carried out relative to equilibrated $CO_2$ gases and a reaction temperature of 90 °C (carbon dioxide equilibrium scale; CDES 90) using the pooled session mode of D47crunch (Daëron, 2021). For data processing, ETH-3 replicates were individually labelled since their $\Delta_{47}$ and $\Delta_{48}$ values have been shown to be compromised by variable amounts of $NO_2$ interferent (Fiebig et al., 2024). This way, ETH-3 is excluded from the variance minimization algorithm of D47crunch (Daëron, 2021) which would otherwise affect $\Delta_{47}$ and $\Delta_{48}$ values of unknown samples (Fiebig et al., 2024). Uncertainties in $\Delta_{47}$ (CDES 90) and $\Delta_{48}$ (CDES 90) reflect fully propagated 2 SE, both considering autogenic and allogenic errors. The revised $\Delta_{47}$-T calibration of Fiebig et al. (2024) was utilized to calculate temperatures. In order to reconstruct seawater $\delta^{18}O$ we used the equation based on molluscs of Grossman and Ku (1986). $\delta^{18}O$ values of $CO_2$ evolved from phosphoric acid digestion of aragonite was converted to $\delta^{18}O_{Arag}$ by applying the acid fractionation equation of Kim et al. (2007) for calcite since Grossman and Ku (1986) originally normalised their calibration data to NBS 19 calcite and, therefore, did not account for differences in acid fractionation factors between aragonite and calcite.

### 3.5. Daydacna – Daily Mg/Ca cycle based internal age model

To determine the ontogenetic age of the clam and to obtain a daily resolved internal age model we used the Python script Daydacna (see Arndt et al., 2023). This script uses wavelet transformation on sub-daily resolved El/Ca data to determine the main daily cycle wavelengths at a given distance along the shell. With the information of daily cycle lengths and the changes therein, an internal growth rate, and thus age model, is calculated. The El/Ca data measured along the distance of the shell are converted onto the time scale, facilitating the interpretation of proxy data regarding the timing of events and cycles.

## 4. Results

### 4.1. Preservation and optical analysis of the shell

The specimen displays signs of alteration on its external shell parts. The umbo is not well preserved, and it is possible that some outermost parts of the shell may be missing, e.g. via minor dissolution (Fig. 1 B). Therefore, it is not possible to analyse the earliest periods of the clam's growth or to determine the exact lifespan of the shell. Despite some visible alteration on the outside (Fig. 1 B), the inner areas appear pristine. Optical investigations of the thin sections confirm this observation, as the outer rim (~1 cm) shows a clear change in colour and at times visible recrystallisation, while the inner part of the shell has an optically pristine appearance, with no signs of recrystallisation or dissolution (Fig. 1 C,D). Additional tests for alteration were conducted using El/Ca data and mineral phase analyses. These indicate that the aragonitic shell mineralogy is preserved within the inner shell area (see Arndt et al., 2023).

Along the entire cross-section of the shell there is a conspicuous light-dark banding pattern (Fig. 1 C,D). In the ontogenically younger part of the shell the banding pattern is irregular, while the ontogenetically older area of the shell displays a more regular banding structure (Fig. 1 D). The daily growth increment structure is partially visible but not continuously discernible throughout the shell.

### 4.2. SIS age

The $^{87}Sr/^{86}Sr$ values of the pristine shell areas are 0.708883 ± 0.000016 (2 SD), whereas visually altered sections reach values of up to 0.708896 ± 0.000019 (2 SD). Altered and pristine values are within error of each other, with the mean $^{87}Sr/^{86}Sr$ of all datasets equal to 0.708895 ± 22 (2 SD) see table S1. Corresponding ages are based on an approximate age from biostratigraphic analyses of the specimen's sampling location (Renema et al., 2015) and were constructed via a cross-correlation with the SIS Look-Up Table (Version 4: 08/04; McArthur et al., 2001; McArthur and Howarth, 2005). The ages are 10.1 ± 0.6 (2 SD) Ma when considering the pristine dataset only, while the altered sections correspond to an apparent age of 9.7 ± 0.7 Ma (2 SD) (Fig. S1).

### 4.3. Internal age model

#### 4.3.1. Age and growth rate determination using sub-daily resolved trace element data

The internal age model based on the evaluation of daily Mg/Ca cycles using the Daydacna programme (see Arndt et al., 2023) yielded an age estimate of 20,916 ± 1220 days (2 SD). Assuming a Miocene year had 365 days, this translates to 57.3 ± 3.3 years (2 SD). Given the size of the data set (628,612 measurements per element) and the need to estimate the uncertainty via Monte Carlo simulations, the entire record was divided into 14 subsets for data processing. Details of the parameters used by Daydacna and the results of each of the individual segments can be found in the supplementary online material (Table S4, Figs. S2-S15). The internal age model, i.e. the distance-time relationship, is displayed in Fig. 3.

#### 4.3.2. Application of the age model to the $\delta^{18}O$ and $\delta^{13}C$ data

Stable oxygen and carbon isotopic compositions were measured from powder milled from slabs, while elemental ratios were obtained from corresponding thin sections. Although the ablation and milling tracks were therefore positioned very close to each other within the shell (a few millimetres apart on opposite slabs), the growth pattern within the shell varies slightly between the two tracks. Furthermore, cracks in the ontogenetically youngest parts prevented the collection of sufficient unaltered powder for reliable oxygen and carbon isotope measurements in these growth areas, while the cracks could be avoided using laser ablation. This results in a slightly shorter isotope record compared to the elemental ratio record. To reduce the potential offset and to increase comparability between the datasets we use the dark bands within the shell as anchor points in order to align the two datasets onto the same distance scale (Fig. 2).

The banding pattern, linked to the stable isotope dataset, was quantified by optical analysis of slab photographs. In the two ontogenetically oldest slabs (numbers 6 and 5) the lower sampling resolution of 0.3 mm allowed us to assign the attribute "dark band" and "light band" to each $\delta^{18}O$ and $\delta^{13}C$ datapoint. The 'quarry-like' sampling at 0.1 mm sampling resolution applied to the ontogenetically younger slabs (numbers 4 to 1) made it difficult to optically distinguish between individual samples on the slab images. Therefore, we evaluated a normalised brightness curve extracted from light microscope images and assigned dark bands wherever brightness values were below 0.6 for 10 consecutive pixels. The attribute "dark band" and "light band" were then assigned to the isotope values by distance along the milled track. We used a fixed threshold (0.6) to recognise dark bands. As such, we cannot exclude the possibility that bands which were slightly darker compared to the surrounding shell, but not dark enough to cross the threshold, may have been missed.

We could not optically determine the nature of the banding pattern at the sites of the sub-daily resolved El/Ca measurements, because in thin sections the differences in brightness between dark and light banding was not sufficient for a clear identification of the bands. Based on the observation that Mg/Ca is elevated in dark bands (Fig. S16, Fig. 2;

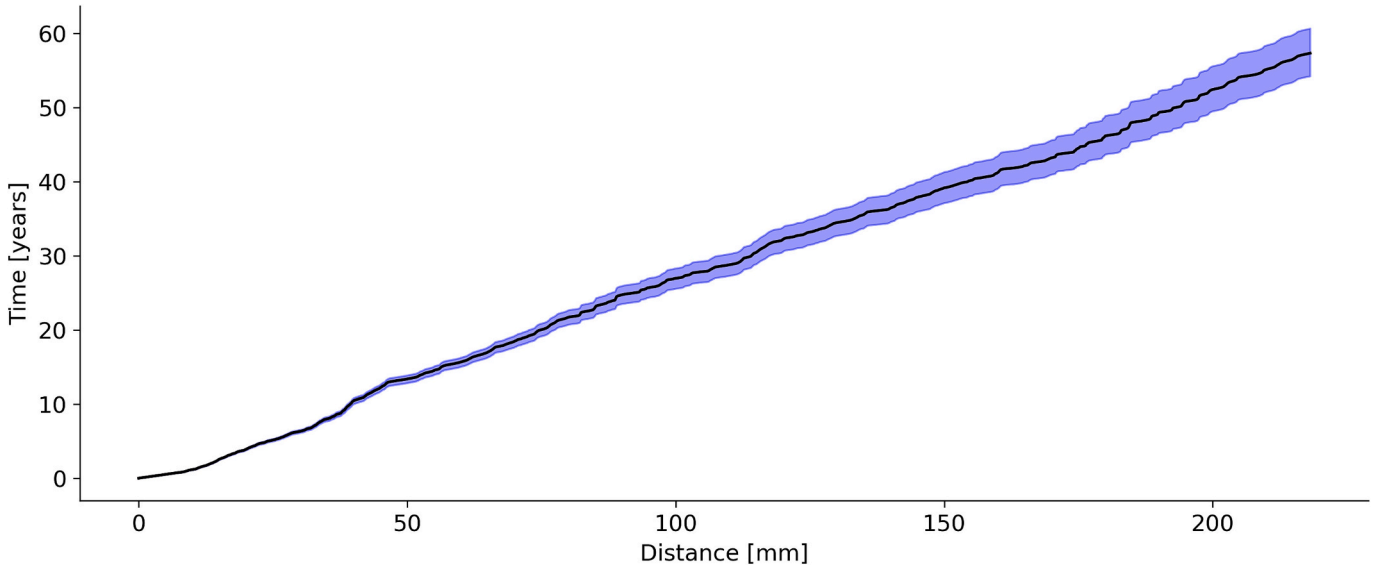


**Fig. 3.** Age model for TOBI with the shaded blue area reflecting the 2.5th to 97.5th percentile interval, indicating 20,916 ± 1220 days (2 SD) or 57.3 ± 3.3 years (2 SD) of growth. Overall, the growth rate is relatively constant throughout the shell apart from seasonal variability. (For interpretation of the references to colour in this figure legend, the reader is referred to the web version of this article.)

see also Arndt et al., 2023), the banding pattern determined for the $\delta^{18}O$ and $\delta^{13}C$ data set could be aligned to the Mg/Ca peaks, defined as maxima with values above the median + 2 SD. The variability of El/Ca relative to the independently determined banding, seen in overview measurements conducted at a lower sampling resolution on the sample slabs, is shown in Fig. S16. The distance value associated with the corresponding Mg/Ca peak centre was matched to the centre of the dark band in the stable isotope data set. Finally, we assigned a new distance value to each isotope value by linearly interpolating between the dark band calibration points, derived by matching the Mg/Ca peaks to the image processing of the micromilled slabs. With the stable isotope dataset now on the elemental ratio distance scale, the distance-time-relationship determined for elemental ratios could be applied to the stable carbon and oxygen isotope data as well.

### 4.4. Elemental ratios

The LA-ICPMS elemental ratio dataset includes 628,612 data points per element, on average equivalent to 10,971 datapoints per year of growth, or ~30 per day. B/Ca values range from 0.01 mmol/mol to 0.14 mmol/mol with an average of 0.05 mmol/mol. The minimum value for Na/Ca is 2.9 mmol/mol, the maximum value 27.9 mmol/mol and the average is 13.2 mmol/mol. Mg/Ca ranges from 0.10 to 1.42 mmol/mol with an average of 0.30 mmol/mol. Average Sr/Ca is 2.1 mmol/mol, with a minimum of 1.1 mmol/mol and narrow peaks which reach values of up to 10.4 mmol/mol. Ba/Ca ranges from 0.5 to 7.2 µmol/mol with an average of 2.4 µmol/mol (Table S5).

To test for multi-annual periodicities in the El/Ca data, multi-taper spectral analysis was performed on 30.42-day (monthly) averaged data using Acycle (Li et al., 2019), with an AR1 process as the null hypothesis (see Fig. S17 for all spectra). One of the significant periodic signals is in the range of 3.6 to 4.4 years and is preserved in B/Ca, Na/Ca and Ba/Ca. Another significant peak occurs between 7.6 and 8.2 years in Na/Ca and Ba/Ca. Furthermore, signals of around 10, 13 and 17 years are seen in B/Ca, Mg/Ca, Sr/Ca and Ba/Ca.

At a seasonal scale, elevated Mg/Ca values coincide with B/Ca and Sr/Ca maxima as well as Na/Ca minima. This pattern is clearly linked to the appearance of dark banding in the shell (Fig. 2) and appears mostly twice per year with varying intensity (Fig. 4 A,B). The pattern shows irregularity with some increases or decreases in El/Ca, present in the form of two or three nearby peaks. These findings are supported by the spectral analysis (Fig. S17), which indicates that an approximately half year periodic signal is present in B/Ca, Na/Ca, Mg/Ca and Sr/Ca, exceeding the 90 % confidence level. Significant annual cyclicity is present in the signals of Na/Ca, Mg/Ca, Sr/Ca and Ba/Ca where some of these elemental ratios also show other significant periodicities around the yearly frequency band (Fig. S17). In addition, sub-seasonal variability in the form of short-term events can be seen in the data. These multi-day events are most prominently seen as Sr/Ca peaks and usually appear in areas of elevated Mg/Ca and dark banding. B/Ca, Na/Ca and Mg/Ca briefly decrease (overall within areas of increased Mg/Ca and B/Ca values) while Ba/Ca increases together with the sharp increase in Sr/Ca (Fig. 4 C,D). In total, we identified this elemental pattern of short-term extreme events with varying intensities 35 times in the dataset, so on average less than once per year. Fourteen events were moderate while the remaining twenty-one showed clear peaks. The events seemed to be clustered and most appear either between 21 and 29 or between 39 and 51 years (Fig. 4).

### 4.5. Isotopic data

#### 4.5.1. Dual clumped isotopes

The eight replicate measurements yielded a mean $\delta^{13}C_{[VPDB]}$ of 3.05 ± 0.40 ‰ (2 SD) and $\delta^{18}O_{Arag[VPDB]}$ of −1.73 ± 0.07 ‰ (2 SD). The clumped isotopic composition ($\Delta_{47}$) based on these replicates is 0.587 ± 0.007 ‰ (2 SE) while the $\Delta_{48}$ value is 0.239 ± 0.021 ‰ (2 SE). The data point plots within uncertainty indistinguishably from the $\Delta_{47}$-$\Delta_{48}$ equilibrium line of Fiebig et al. (2024) (Fig. 5), indicating growth in isotopic equilibrium and validating the suitability of $\Delta_{47}$ as a reliable temperature proxy in *Tridacna*. The temperature calculated from the $\Delta_{47}$ value ±2 SE lies between 25.6 and 30.3 °C with a mean of 27.9 °C (Table S6). By inserting the clumped isotope derived temperature into the empirical temperature-$\delta^{18}O_{sw}$-$\delta^{18}O_{Arag}$ relationship for aragonitic molluscs of Grossman and Ku (1986), we calculated a $\delta^{18}O_{sw\ [SMOW]}$ of −0.43 ± 0.50 ‰ for this late Miocene location.

#### 4.5.2. Stable oxygen and carbon isotopes

$\delta^{18}O_{Arag}$ on the shell age model shows a broadly cyclic variability between −2.86 ‰ and -1.27 ‰ with a mean of −2.16 ‰ (Fig. 6 A). The cyclicity is typically approximately yearly (Fig. 6 B). $\delta^{13}C$ values range from 2.06 ‰ to 3.60 ‰ with a mean of 2.99 ‰ (Table S7). No distinct yearly signal can be observed in $\delta^{13}C$, however multi-annual cycles are

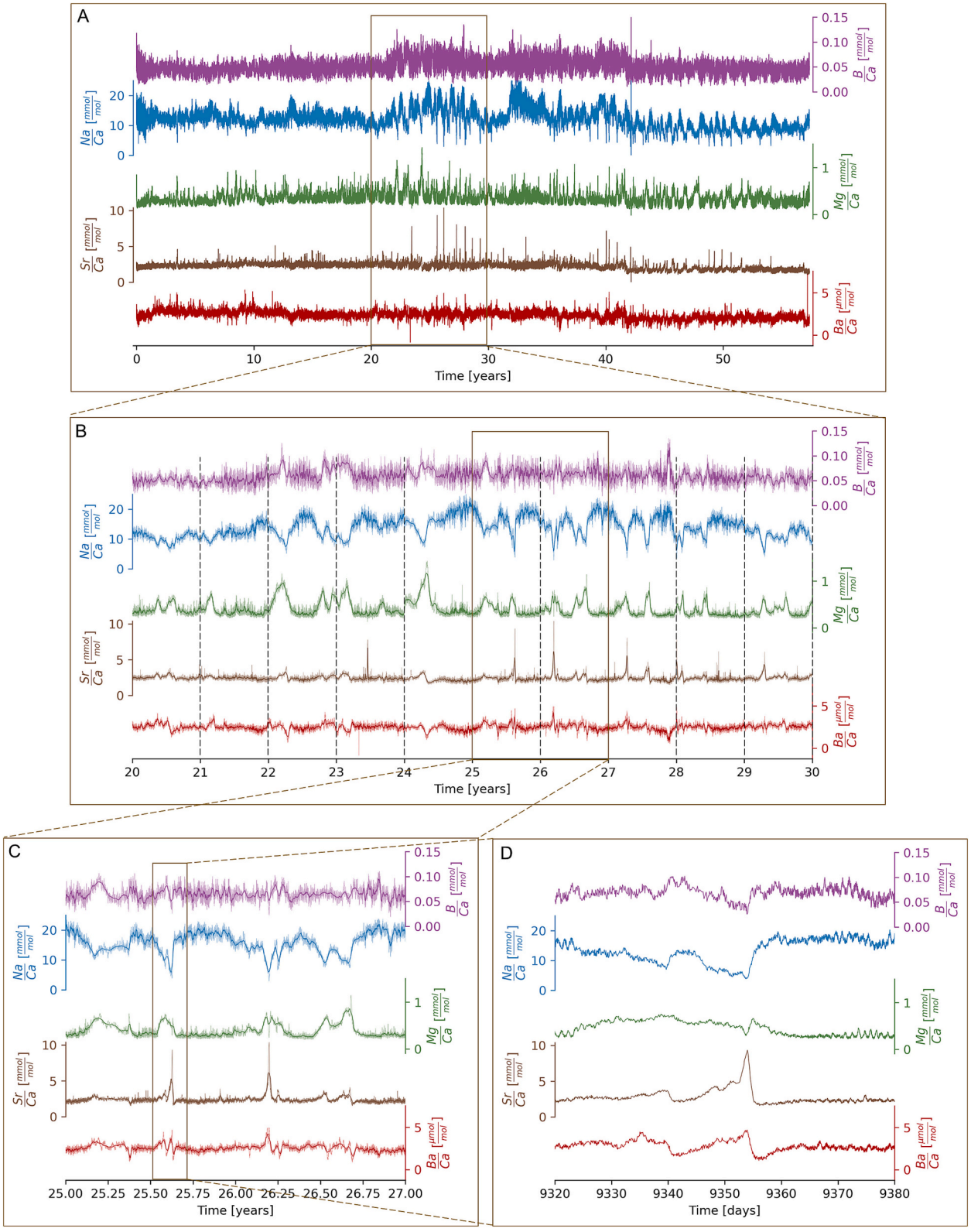


**Fig. 4.** Elemental ratios versus time. A: Overview over the entire record of ~250 mm, representing ~57 years. Cyclicities are seen in all elemental ratios. While B/Ca, Mg/Ca and Sr/Ca positively co-vary, Na/Ca is anticorrelated with the other trace element ratios. Ba/Ca is characterised by a less regular pattern, with several peaks in phase with B/Ca, Mg/Ca and Sr/Ca. B: Close-up of the section from 20 to 30 years, highlighting the consistent presence of two peaks or troughs per year. C: Close-up of the section of 25 to 27 years to highlight the presence of short seasonal peaks, most clearly visible in Sr/Ca. D: Close-up of a ~two-months period, namely 9320 to 9380 days (25.53 to 25.70 years), with a 38-day-long seasonal peak spanning from about 9323 to 9360 days and one short-term event spanning over 3 days (from 9353 to 9356), represented by a positive peak in Sr/Ca and Ba/Ca and correspondingly negative Mg/Ca, Na/Ca, and B/Ca excursions. Daily cycles are visible particularly well between 9370 and 9380 days.

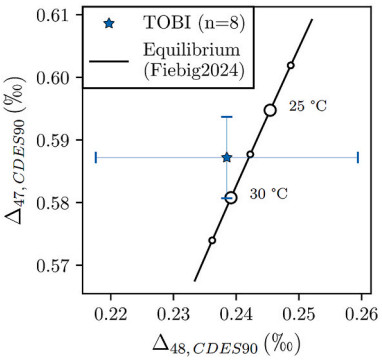


**Fig. 5.** Dual clumped isotope ($\Delta_{47}$, $\Delta_{48}$) space. The late Miocene Tridacna sample TOBI lies within fully error propagated 2 SE of the proposed $\Delta_{47}/\Delta_{48}$ temperature equilibrium relationship of Fiebig et al. (2024).

present (Fig. 6 A). No clear link with the banding pattern is visible in the case of either $\delta^{18}O_{Arag}$ or $\delta^{13}C$ as both minima and maxima can occur in dark bands.

The spectral analysis of the monthly binned $\delta^{18}O_{Arag}$ and $\delta^{13}C$ data shows that a yearly periodicity is present with 90 % confidence over an AR(1) null hypothesis in the $\delta^{18}O_{Arag}$ but not the $\delta^{13}C$ dataset. Regarding long-term variabilities, $\delta^{18}O_{Arag}$ shows significant periodicities at 4.6 and 7.6 years, while $\delta^{13}C$ shows significant periodicities at 3.9 and 4.4 years as well as at 7 and 8.3 years (Fig. S17).

Using the temperature equation for aragonitic molluscs from Grossman and Ku (1986), and a constant $\delta^{18}O_{sw}$ of −0.43 ‰ (derived via dual clumped isotope measurements), we arrive at an apparent seasonal temperature range of 23.8 to 31.3 °C (see discussion).

#### 4.5.3. *Strontium isotopes*

The seasonally-resolved strontium isotopic data of the shell were measured across three years of growth, covering six light areas and six dark bands. We found no difference in $^{87}Sr/^{86}Sr$ between the dark bands with 0.708904 ± 0.000021 (2 SD) and light bands with 0.708903 ± 0.000014 (2 SD) (Table S2). Furthermore, all twelve measurements are within error of each other and indistinguishable from the SIS value of 0.708883 ± 0.000016 (2 SD) (Fig. S18).

## 5. Discussion

The multiproxy dataset presented in this study spans nearly six decades at sub-daily to seasonal resolution. It provides insights not only into multi-annual but also seasonal and shorter-term aspects of late Miocene tropical climate in the Indo-Pacific region. This is, to the best of our knowledge, the first sub-daily resolved, multi-decadal record identifying sub-seasonal patterns in a tropical palaeoenvironment.

For specimens like our late Miocene *Tridacna* TOBI, for which daily banding could not be resolved optically throughout the entire shell, daily geochemical cycles are more reliable indicators of daily growth (Arndt et al., 2023). Prior research has revealed that daily cycles occur in Sr/Ca and Mg/Ca of *Tridacna* shells and are possibly linked to the light-dependent incorporation of these elements in the shell, which could be induced by daily variability in photosymbiotic activity (Sano et al., 2012; Warter and Müller, 2017; Warter et al., 2018) and/or light-enhanced calcification (Rossbach et al., 2019; Sano et al., 2012). In a previous *Tridacna* culturing study, Warter et al. (2018) demonstrated that the number of bands and El/Ca cycles was equal to the culturing period in days. We found that the Mg/Ca cycles in our sample, ranging from a few to tens of µm, align well with the microscopical banding pattern where it is visible (Arndt et al., 2023). Because of the similarity of our observations to that from the cultured *Tridacna* in Warter et al. (2018) we are confident that daily El/Ca cycles are preserved in our fossil sample. Our Python based script Daydacna (Arndt et al., 2023; Arndt and Coenen, 2023) can create an internal age model for long datasets and is likely to be useful even in cases of good increment visibility, as cycle quantification is semi-automated and there is no need for counting (tens of) thousands of daily increments. Converting data from

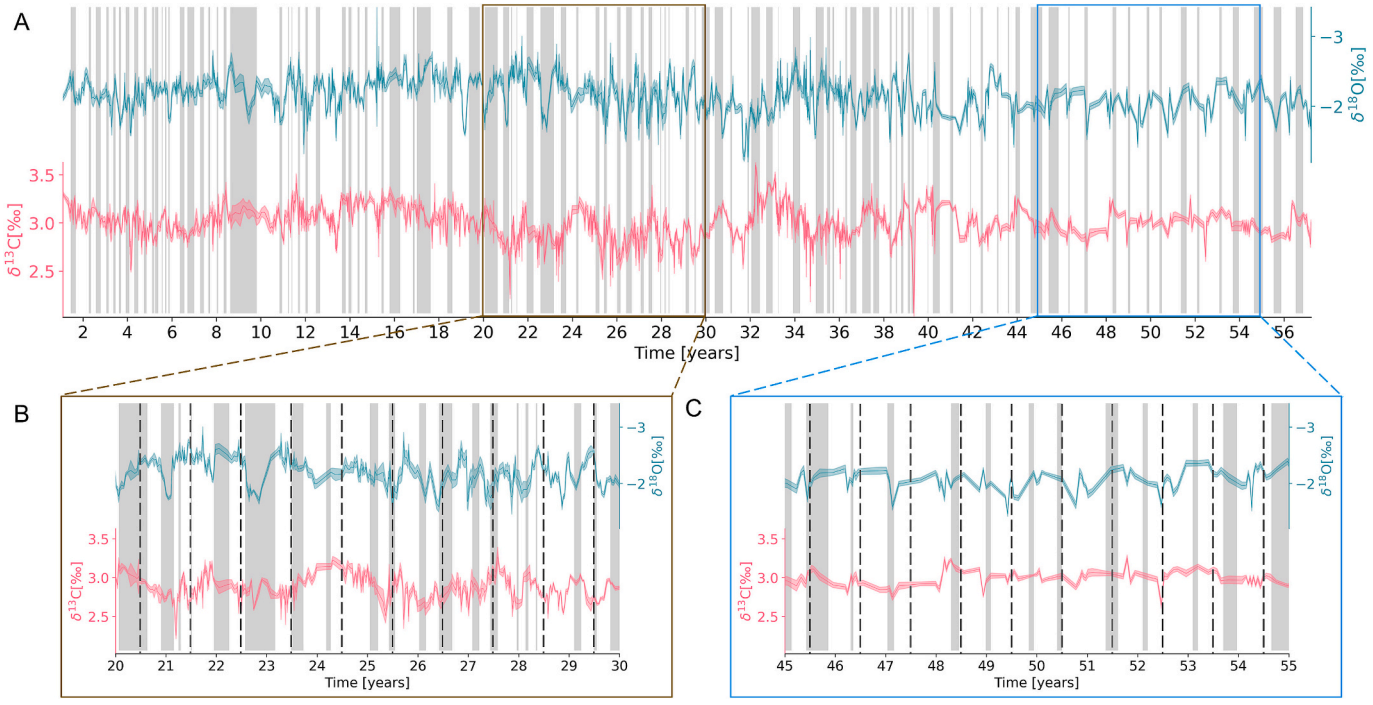


**Fig. 6.** A: Stable carbon and oxygen isotope variability as a function of relative growth time across the shell. The shaded areas reflect the uncertainty (2 SD). The first year could not be sampled (see the section on preservation). The grey bars indicate position and width of the visible dark bands transferred to the time scale. B: Closeup of the section of 20 to 30 years with vertical lines indicating the middle of each year. $\delta^{18}O_{Arag\ [VPDB]}$ values show asymmetric yearly cycles while $\delta^{13}C_{[VPDB]}$ cycles are multi-annual. C: Closeup of the section of 45 to 55 years. At the lower sampling resolution (300 µm steps, seasonal resolution) cycles are less clear.

the distance to the time scale facilitates both timing and duration of multi-annual, seasonal or short-term events to be elucidated in the elemental and isotopic record and can help to understand the connection between shell growth, shell structure and proxy data.

### 5.1. Equilibrium calcification, temperature and $\delta^{18}O_{sw}$ derived from dual clumped isotopes

Through dual clumped isotope analysis, we are able to verify the assumption that *Tridacna* calcify in isotopic equilibrium, which has only previously been inferred based on observations of modern *Tridacna* shells, in which measured $\delta^{18}O_{sw}$ and temperature values match the respective values calculated via $\delta^{18}O_{Arag}$ (e.g. Aharon and Chappell, 1986; Arias-Ruiz et al., 2017; Duprey et al., 2015; Elliot et al., 2009). Furthermore, this finding demonstrates that the isotopic signature was not significantly impacted by open-system diagenesis e.g. through heating and fluid-carbonate interaction with isotopically distinct diagenetic fluids, as this could result in an offset from the equilibrium curve (Staudigel et al., 2023a, 2023b). The resulting temperature, independent of assumptions of the oxygen isotopic composition of seawater, of 27.9 ± 2.4 °C (2 SE) is similar to modern temperatures in the region (e.g. Purwandari et al., 2019; Teichberg et al., 2018). The calculated mean $\delta^{18}O_{sw}$ of −0.43 ± 0.50 ‰, reconstructed from the clumped isotope derived temperature, is in agreement with previous reconstructions of late Miocene $\delta^{18}O_{sw}$ (Lear et al., 2000; Rohling et al., 2022).

### 5.2. Multi-annual cycles

Overall, the multi-annual variabilities in elemental and isotopic ratios are not very pronounced. However, the two clearly resolvable periodicities, especially in the $\delta^{18}O_{Arag}$, $\delta^{13}C$, B/Ca, Na/Ca and Ba/Ca time-series, include significant signals between 3.6 and 4.6 as well as 7 to 8.2 years. In the modern ocean, the El Niño climate phenomenon typically occurs every two to seven years (McPhaden et al., 2020) and is linked to weaker easterly trade winds through a weakened Walker circulation, reduced precipitation in the West Pacific and a weakened and cooler ITF (Ffield et al., 2000; Timmermann et al., 2018; Yamanaka et al., 2018; Zhang et al., 2016). Similarly, in the late Miocene, ENSO like ocean-atmosphere dynamics appear to have affected precipitation patterns and the ITF strength, inducing changes in the water currents flowing into the reef and thus impacting local temperature, seawater isotopic composition and nutrient availability, all recorded in the shell geochemistry. Owing to their longevity, modern and Holocene specimens of *Tridacna* have already been shown to be a suitable archive for recording ENSO variabilities in the $\delta^{18}O$ composition of the shell (Shao et al., 2020; Welsh et al., 2011). Our findings affirm the previously suggested hypothesis that ENSO was present in the late Miocene, following the formation of an incipient Indo-Pacific proto-warm pool with a La Niña-like mean state as early as 11.6 Ma (Nathan and Leckie, 2009; Batenburg et al., 2011; Sosdian and Lear, 2020; Fox et al., 2021; Gallagher et al., 2024).

### 5.3. Seasonal cycles

Seasonal patterns are visible in the $\delta^{18}O_{Arag}$ profiles which display yearly cyclicity, as well as in some El/Ca datasets, which show a pattern of two peaks per year, some of which are double peaks. Amongst the El/Ca data, the seasonal peaks are most clearly seen as positive Mg/Ca and Sr/Ca as well as negative Na/Ca peaks (Fig. 4). Increased Mg/Ca in *Tridacna* has previously been linked to elevated temperatures (Arias-Ruiz et al., 2017; Ayling et al., 2015; Warter et al., 2015), reduced light availability and physiological stress, especially on short (daily) time scales (Warter et al., 2018), as well as reduced growth rates (Arndt et al., 2023). Similarly, studies on other bivalves indicate elevated Mg/Ca in areas of reduced growth (Schleinkofer et al., 2021) and increased organic content (Schleinkofer et al., 2021; Schöne et al., 2010). Observations regarding Sr/Ca in *Tridacna* are ambiguous, some studies indicate that Sr/Ca is correlated to SST (Mei et al., 2018; Yan et al., 2013; Yan, 2020) while others have shown no significant correlation between Sr/Ca and SST (Arias-Ruiz et al., 2017; Batenburg et al., 2011; Elliot et al., 2009; Warter et al., 2018). Like Mg/Ca, Sr/Ca is known to be affected by diurnal changes in solar irradiance (Hori et al., 2015; Sano et al., 2012) and physiological performance and growth (Carré et al., 2006; Gillikin et al., 2005; Warter et al., 2018). Na plays a role for calcification in *Tridacna* as $Na^+/K^+$ -ATPase maintains the gradient of these molecules between the calcification site and cytosol of the adjacent cells, while $Na^+/Ca^{2+}$ exchangers maintain charge balance by removing $Na^+$ from the calcifying fluid to provide $Ca^{2+}$ for calcification (Boo et al., 2019; Boo et al., 2017). Na/Ca could be affected by kinetics and the concentration of the ions in the extrapallial fluid, dependent on ion input through ion exchange and ion deposition into the shell during calcification. Low Na/Ca occur during low growth rate phases characterised by elevated Mg/Ca, which implies that the Ca concentration in the extrapallial fluid could be enriched relatively to Na, inducing low Na/Ca in the shell. However, more research on Na/Ca in *Tridacna* shells grown in controlled settings is needed to fully understand the causes for Na/Ca variability and its implications. Similarly, B/Ca is not established as an unambiguous environmental or physiological performance proxy in *Tridacna.* However, recent studies on *Arctica islandica* show significant negative correlation between shell B/Ca and temperature (Schöne et al., 2023), which may have a mechanistic basis via the impact that temperature has on physiological processes that control the calcification site borate/carbon dynamics.

The strong peaks in Mg/Ca and Sr/Ca coupled to low growth rates in our sample could be caused by the seasonal passing of the ITCZ over the near-equator reef twice a year. While the ITCZ had its northernmost seasonal position near the equator at 15 Ma, it shifted northwards during the late Miocene and reached a seasonal northernmost position of ~10° N at 8 Ma (Groeneveld et al., 2017). The passage of the ITCZ would be coupled to cloudy and rainy conditions, which would reduce both solar irradiation onto the sea surface and induce reduced growth rates in the photosymbiont-bearing tridacnids. In the present, the complex, regional precipitation patterns in the Indo-Pacific are driven by rainy seasons, linked to the ITCZ situated above the location and air convection being at its strongest (Yuan et al., 2023). Recent monitoring from Baik and Triangle reefs in Darvel Bay, situated on the eastern shore of Borneo (Macassar Strait) at 5° N (Mills et al., 2023), indicates that precipitation peaks around November–January and May–July in the years 2018 to 2020, while light availability was high and cloud cover low in February–April and August–October, which corresponds to relatively elevated temperatures. The authors suggested that seasonal turbidity can negatively influence Tridacna growth (Mills et al., 2023). In our data, Ba/Ca are most variable during these periods of elevated Mg/Ca and Sr/Ca. Ba/Ca has been suggested as a potential proxy for riverine influx (Elliot et al., 2009) and primary productivity in *Tridacna* (Arias-Ruiz et al., 2017; Elliot et al., 2009; Hori et al., 2015) and other molluscs (Fröhlich et al., 2022; Gillikin et al., 2008; Marali et al., 2017), and short-term Ba/Ca peaks have been introduced as indicators for storm events in *Tridacna* (Komagoe et al., 2018), and tsunamis in other mussels (Sano et al., 2021). During the rainy season, increased precipitation induces more run-off which increases nutrient availability for primary productivity, while the cloudy conditions and thus reduced solar irradiation inhibit primary productivity. Regional short-term changes in this balance could cause increased primary productivity variability, reflected in our sample's Ba/Ca. We do not expect that seasonal differences in riverine influx strongly affected the reef, as we would expect more pronounced Ba/Ca peaks than observed, potentially including seasonal changes in $^{87}Sr/^{86}Sr$ in such a scenario. Even though El/Ca proxies in *Tridacna*, and marine bivalves in general, can often not be linked to a single environmental factor and are partially physiologically determined (Schöne et al., 2023; Warter et al., 2018), the overall observations of

environmental settings causing El/Ca excursions as described above combined with the regional setting in which the clam grew, make it probable that the seasonal elemental variability observed in our sample is a recorder of the cloudier rainy season linked to the ITCZ passing.

The yearly $\delta^{18}O_{Arag}$ variation could be induced by temperature and/or $\delta^{18}O_{sw}$ changes. The mean $\delta^{18}O_{sw}$ value of −0.43 ‰, derived from the clumped isotope temperature and $\delta^{18}O_{Arag}$, is higher than the previously assumed $\delta^{18}O_{sw}$ value of −0.88 ‰ for the Miocene tropics (Batenburg et al., 2011) but reflects the reconstructed late Miocene whole ocean $\delta^{18}O_{sw}$ value of around −0.5 ‰ (Lear et al., 2000; Rohling et al., 2022). If the $\delta^{18}O_{sw}$ value was seasonally constant, the temperature range necessary to explain the observed intra-shell $\delta^{18}O$ heterogeneity would be over 7 °C. The typical seasonal cyclic $\delta^{18}O_{Arag}$ range is <1 ‰, which would indicate typical intra-annual temperature ranges of 26 to 30 °C. This range is larger than recent seasonal SST variability of about 2 °C in the Makassar strait (e.g. Purwandari et al., 2019; Teichberg et al., 2018).

It is likely that part of the $\delta^{18}O_{Arag}$ variability is induced by $\delta^{18}O_{sw}$ changes due to regional evaporation, precipitation or changes in the isotopic composition of the water flowing into the reef. Changes in both temperature and $\delta^{18}O_{sw}$ can be induced through changes of water entering the reef either through runoff from land, upwelling and/or changes in surface currents. The sample grew in the Makassar strait, which is an essential part of the ITF, through which water flows southwards from the Pacific into the Indian Ocean. The passing of the ITCZ and the connected change in wind forcing influences the flow, temperature and salinity of the ITF (Kuhnt et al., 2004). Such changes could have affected the flow of water currents regionally, thus potentially impacting water temperature and isotopic signatures in the late Miocene reef environment TOBI grew in, leading to the irregular annual $\delta^{18}O_{Arag}$ cycles recorded in the shell.

### 5.4. Short-term events

Short-term events, spanning a few days only, are most prominently seen as Sr/Ca peaks (Fig. 4), with concomitant, yet less-pronounced peaks in Ba/Ca, while Mg/Ca, Na/Ca and B/Ca show negative excursions (Fig. 4 C,D). These events, with durations of a few days only, occur within the overall elevated Mg/Ca dark band areas grown during the rainy season. We hypothesise that they indicate extreme weather events, most likely characterised by very heavy precipitation, as *Tridacna* have been shown to record such events in their elemental composition, e.g. in Ba/Ca (Komagoe et al., 2018). The coincident increase in Sr/Ca and Ba/Ca could indicate increased runoff from land, linked to increased turbidity in the reef and reduced light availability, while decreased Mg/Ca and B/Ca might be an indicator of reduced water temperatures. Finally, we note that Mg/Ca heterogeneity in bivalve shells has also been linked to crystal structure (Schöne et al., 2013). It is therefore also possible that the recorded Mg/Ca drop in our sample is crystal structure related (i.e., controlled by kinetic processes), because these short-term events visibly impact the structure of the clam shell (Fig. S19). We cannot completely rule out the possibility of very short growth hiati during the extreme weather events, although giant clams are considered to have continuous growth throughout the year (Schwartzmann et al., 2011) and have recently been shown to continue growing during short extreme events such as heat waves (Fousiya et al., 2024). Furthermore, the presence of yearly and half-yearly cycles in the spectral analysis (Fig. S17) indicate that these events are very likely not connected to longer growth hiati (spanning weeks or more).

## 6. Conclusion and Outlook

This contribution affirms the importance of giant clams for reconstructing pre-Pleistocene palaeoclimates by presenting the first, to our knowledge, multi-decadal (57 ± 3 years), multi-proxy record from a giant clam at daily time resolution. Using this record from a late Miocene tropical reef, we provide insights into climate patterns on multi-annual, seasonal and daily time scales across several decades, in addition to reconstructing the occurrence of short-term extreme weather events in a late Miocene tropical reef. Multi-annual periodicities of around four years suggest atmosphere-ocean interactions akin to multi-annual cyclic climate patterns like today's ENSO system. On a (sub-)annual scale, we observed two key periodicities. The first cycle is visible as yearly variability in $\delta^{18}O_{Arag}$ indicating changes in temperature and/or $\delta^{18}O_{sw}$, likely linked to different water currents entering the reef. The second intra-annual pattern consists of peaks in elemental ratios occurring approximately twice a year, which we interpret as being driven by a cloudy and rainy seasonal signal coupled to the passing of the ITCZ over the equatorial reef twice a year. In addition, we found 35 short-term extreme weather events across ~57 years, most clearly seen in Sr/Ca peaks, likely indicating short-term heavy precipitation events during the rainy season, linked to increased runoff and turbidity in the reef. Finally, our dual clumped isotope results demonstrate that our *Tridacna* sample calcified, within uncertainty, in isotopic equilibrium, enabling us to reconstruct average SST at 10 Ma of ~28 °C and a mean $\delta^{18}O_{sw}$ of around −0.4 ‰. Future studies may include seasonal clumped isotope analysis to better deconvolve the seasonal temperature and $\delta^{18}O_{sw}$ changes (see e.g. de Winter et al., 2021; Kniest et al., 2024).

While the multi-decadal nature of our data set shows that these patterns hold true over long time spans and do not simply reflect a few unusual years, our sample represents one snapshot in time at one locality. More datasets such as this are required to assess local effects and gain a deeper understanding of past seasonality and extreme weather patterns on a larger scale. We suggest that future studies could follow this approach of placing highly resolved geochemical data onto an internal age model, as it has great potential to help understanding past seasonality and palaeo-weather. Ultimately, we envision that a network of such datasets from the same time interval could be used to map multi-annual and seasonal climate phenomena like ENSO activity and past ITCZ positions, while a comparison over time can provide information on the shifts in seasonality and frequency of extreme weather events in a changing climate. Finally, such (sub-)seasonal climate time series are crucial not only for a deeper understanding of past climate systems but also to test the skill of climate models (Carré and Cheddadi, 2017; Cauquoin et al., 2019; Schmidt et al., 2014; Tierney et al., 2020).

## CRediT authorship contribution statement

**Iris Arndt:** Writing – review & editing, Writing – original draft, Visualization, Validation, Software, Methodology, Investigation, Funding acquisition, Formal analysis, Data curation, Conceptualization. **Miguel Bernecker:** Writing – review & editing, Visualization, Validation, Software, Methodology, Investigation, Formal analysis, Data curation. **Tobias Erhardt:** Investigation, Writing – review & editing. **David Evans:** Writing – review & editing, Validation, Supervision, Investigation. **Jens Fiebig:** Writing – review & editing, Validation, Resources, Methodology, Funding acquisition, Conceptualization. **Maximilian Fursman:** Writing – review & editing, Validation. **Jorit Kniest:** Writing – review & editing, Validation. **Willem Renema:** Writing – review & editing, Validation, Resources, Conceptualization. **Vanessa Schlidt:** Writing – review & editing, Validation, Conceptualization. **Philip Staudigel:** Writing – review & editing, Validation, Investigation. **Silke Voigt:** Data curation, Methodology, Visualization, Writing – review & editing, Validation. **Wolfgang Müller:** Writing – review & editing, Validation, Supervision, Resources, Project administration, Methodology, Investigation, Funding acquisition, Data curation, Conceptualization.

## Declaration of competing interest

The authors declare the following financial interests/personal relationships which may be considered as potential competing interests:

Iris Arndt reports financial support was provided by German

Research Foundation. Wolfgang Muller reports financial support was provided by German Research Foundation. If there are other authors, they declare that they have no known competing financial interests or personal relationships that could have appeared to influence the work reported in this paper.

## Data availability

All data sets presented in this study are available as tables S1 to S7 at Zenodo with licence CC BY 4.0 (https://doi.org/10.5281/zenodo.14609845).

## Acknowledgements

We would like to thank the Stiftung Polytechnische Gesellschaft as well as the Deutsche Forschungsgemeinschaft grant (DFG MU 3739/6-1) for providing financial support for the corresponding author (IA). We are grateful for the expert sample preparation conducted by Maria Bladt, Sören Tholen and Niels Prawitz, as well as technical support of Linda Marko, Alexander Schmidt and Richard Albert during LA-ICPMS and solution MC-ICPMS measurements, data reduction and microscope imaging. We further thank Christian Bredefeld for help with micromilling and Sven Hoffmann for technical assistance and stable isotope measurements. Manuel Schumann and Phil Dolz are thanked for preparing equilibrated gas standards. Discussions with Douglas Coenen clarified aspects of time-series analysis and Python coding. The VeWA consortium (Past Warm Periods as Natural Analogues of our high-$CO_2$ Climate Future) by the LOEWE programme of the Hessen Ministry of Higher Education, Research and the Arts, Germany, co-funded aspects of this research (DE, WM). FIERCE is financially supported by the Wilhelm and Else Heraeus Foundation and by the Deutsche Forschungsgemeinschaft (DFG: INST 161/921-1 FUGG, INST 161/923-1 FUGG and INST 161/1073-1 FUGG), which is gratefully acknowledged. This is FIERCE contribution No. 186. We thank the editors and two anonymous reviewers for their valuable comments on an earlier version of this manuscript, which helped to improve both content and presentation.

## Appendix A. Supplementary data

Supplementary data to this article can be found online at https://doi.org/10.1016/j.palaeo.2024.112711.

## References

Aharon, P., Chappell, J., 1986. Oxygen isotopes, sea level changes and the temperature history of a coral reef environment in New Guinea over the last 105 years. Palaeogeogr. Palaeoclimatol. Palaeoecol. 56, 337–379. https://doi.org/10.1016/0031-0182(86)90101-X.

Arias-Ruiz, C., Elliot, M., Bézos, A., Pedoja, K., Husson, L., Cahyarini, S.Y., Cariou, E., Michel, E., La, C., Manssouri, F., 2017. Geochemical fingerprints of climate variation and the extreme La Niña 2010–11 as recorded in a *Tridacna squamosa* shell from Sulawesi, Indonesia. Palaeogeogr. Palaeoclimatol. Palaeoecol. 487, 216–228. https://doi.org/10.1016/j.palaeo.2017.08.037.

Arndt, I., Coenen, D., 2023. Daydacna. https://doi.org/10.5281/ZENODO.8334594.

Arndt, I., Coenen, D., Evans, D., Renema, W., Müller, W., 2023. Quantifying sub-seasonal growth rate changes in Fossil Giant Clams using Wavelet Transformation of Daily Mg/Ca Cycles. Geochem. Geophys. Geosyst. 24. https://doi.org/10.1029/2023GC010992 e2023GC010992.

Ayling, B.F., Chappell, J., Gagan, M.K., McCulloch, M.T., 2015. ENSO variability during MIS 11 (424–374 ka) from *Tridacna gigas* at Huon Peninsula, Papua New Guinea. Earth Planet. Sci. Lett. 431, 236–246. https://doi.org/10.1016/j.epsl.2015.09.037.

Batenburg, S.J., Reichart, G.-J., Jilbert, T., Janse, M., Wesselingh, F.P., Renema, W., 2011. Interannual climate variability in the Miocene: High resolution trace element and stable isotope ratios in giant clams. Palaeogeogr. Palaeoclimatol. Palaeoecol. 306, 75–81. https://doi.org/10.1016/j.palaeo.2011.03.031.

Bernasconi, S.M., Daëron, M., Bergmann, K.D., Bonifacie, M., Meckler, A.N., Affek, H.P., Anderson, N., Bajnai, D., Barkan, E., Beverly, E., Blamart, D., Burgener, L., Calmels, D., Chaduteau, C., Clog, M., Davidheiser-Kroll, B., Davies, A., Dux, F., Eiler, J., Ziegler, M., 2021. InterCarb: a community effort to improve interlaboratory standardization of the carbonate clumped isotope thermometer using carbonate standards. Geochem. Geophys. Geosyst. 22 (5). https://doi.org/10.1029/2020GC009588.

Bernecker, M., Hofmann, S., Staudigel, P.T., Davies, A.J., Tagliavento, M., Meijer, N., Ballian, A., Fiebig, J., 2023. A robust methodology for triple ($\Delta_{47}$, $\Delta_{48}$, $\Delta_{49}$) clumped isotope analysis of carbonates. Chem. Geol. 642, 121803. https://doi.org/10.1016/j.chemgeo.2023.121803.

Betzler, C., Eberli, G., Lüdmann, T., Reolid, J., Kroon, D., Reijmer, J., Swart, P., Wright, J., Young, J., Zarikian, C., Alonso Garcia, M., Bialik, O., Blättler, C., Guo, J., Haffen, S., Horozal, S., Inoue, M., Jovane, L., Lanci, L., Yao, Z., 2018. Refinement of Miocene Sea level and monsoon events from the sedimentary archive of the Maldives (Indian Ocean). Prog. Earth Planet Sci. 5, 5. https://doi.org/10.1186/s40645-018-0165-x.

Bonham, K., 1965. Growth Rate of Giant Clam Tridacna gigas at Bikini Atoll as Revealed by Radioautography. Science 149, 300–302. https://doi.org/10.1126/science.149.3681.300.

Boo, M.V., Hiong, K.C., Choo, C.Y.L., Cao-Pham, A.H., Wong, W.P., Chew, S.F., Ip, Y.K., 2017. The inner mantle of the giant clam, *Tridacna squamosa*, expresses a basolateral $Na^+/K^+$-ATPase α-subunit, which displays light-dependent gene and protein expression along the shell-facing epithelium. PLoS One 12, e0186865. https://doi.org/10.1371/journal.pone.0186865.

Boo, M.V., Hiong, K.C., Wong, W.P., Chew, S.F., Ip, Y.K., 2019. Shell formation in the giant clam, *Tridacna squamosa*, may involve an apical $Na^+/Ca^{2+}$ exchanger 3 homolog in the shell-facing epithelium of the whitish inner mantle, which displays light-enhanced gene and protein expression. Coral Reefs 38, 1173–1186. https://doi.org/10.1007/s00338-019-01848-y.

Carré, M., Cheddadi, R., 2017. Seasonality in long-term climate change. Quat. Rev. Assoc. Fr. Pour Létude Quat. 28, 173–177. https://doi.org/10.4000/quaternaire.8018.

Carré, M., Bentaleb, I., Bruguier, O., Ordinola, E., Barrett, N.T., Fontugne, M., 2006. Calcification rate influence on trace element concentrations in aragonitic bivalve shells: evidences and mechanisms. Geochim. Cosmochim. Acta 70, 4906–4920. https://doi.org/10.1016/j.gca.2006.07.019.

Caswell, T.A., Droettboom, M., Lee, A., de Andrade, E.S., Hoffmann, T., Klymak, J., Hunter, J., Firing, E., Stansby, D., Varoquaux, N., Nielsen, J.H., Root, B., May, R., Elson, P., Seppänen, J.K., Dale, D., Lee, J.-J., McDougall, D., Straw, A., Hobson, P., Hannah Gohlke, C., Vincent, A.F., Yu, T.S., Ma, E., Silvester, S., Moad, C., Kniazev, N., Ernest, E., Ivanov, P., 2022. Matplotlib/Matplotlib: REL: v3.5.2. https://doi.org/10.5281/zenodo.6513224.

Cauquoin, A., Werner, M., Lohmann, G., 2019. Water isotopes – climate relationships for the mid-Holocene and preindustrial period simulated with an isotope-enabled version of MPI-ESM. Clim. Past 15, 1913–1937. https://doi.org/10.5194/cp-15-1913-2019.

Daëron, M., 2021. full propagation of analytical uncertainties in $\Delta_{47}$ measurements. Geochem. Geophys. Geosyst. 22. https://doi.org/10.1029/2020GC009592 e2020GC009592.

de Winter, N.J., Goderis, S., Malderen, S.J.M.V., Sinnesael, M., Vansteenberge, S., Snoeck, C., Belza, J., Vanhaecke, F., Claeys, P., 2020a. Subdaily-scale chemical variability in a *Torreites Sanchezi* Rudist Shell: implications for rudist Paleobiology and the cretaceous day-night cycle. Paleoceanogr. Paleoclimatol. 35. https://doi.org/10.1029/2019PA003723 e2019PA003723.

de Winter, N.J., Ullmann, C.V., Sørensen, A.M., Thibault, N., Goderis, S., Van Malderen, S.J.M., Snoeck, C., Goolaerts, S., Vanhaecke, F., Claeys, P., 2020b. Shell chemistry of the boreal Campanian bivalve *Rastellum diluvianum* (Linnaeus, 1767) reveals temperature seasonality, growth rates and life cycle of an extinct cretaceous oyster. Biogeosciences 17, 2897–2922. https://doi.org/10.5194/bg-17-2897-2020.

de Winter, N.J., Müller, I.A., Kocken, I.J., Thibault, N., Ullmann, C.V., Farnsworth, A., Lunt, D.J., Claeys, P., Ziegler, M., 2021. Absolute seasonal temperature estimates from clumped isotopes in bivalve shells suggest warm and variable greenhouse climate. Commun. Earth Environ. 2, 1–8. https://doi.org/10.1038/s43247-021-00193-9.

Duprey, N., Lazareth, C.E., Dupouy, C., Butscher, J., Farman, R., Maes, C., Cabioch, G., 2015. Calibration of seawater temperature and $\delta^{18}O_{seawater}$ signals in *Tridacna maxima's* $\delta^{18}O_{shell}$ record based on in situ data. Coral Reefs 34, 437–450. https://doi.org/10.1007/s00338-014-1245-z.

Elliot, M., Welsh, K., Chilcott, C., McCulloch, M., Chappell, J., Ayling, B., 2009. Profiles of trace elements and stable isotopes derived from giant long-lived *Tridacna gigas* bivalves: potential applications in paleoclimate studies. Palaeogeogr. Palaeoclimatol. Palaeoecol. 280, 132–142. https://doi.org/10.1016/j.palaeo.2009.06.007.

Evans, D., Müller, W., 2018. Automated extraction of a Five-Year LA-ICP-MS trace element data set of ten common glass and carbonate reference materials: long-term data quality, optimisation and laser cell homogeneity. Geostand. Geoanal. Res. 42, 159–188. https://doi.org/10.1111/ggr.12204.

Evans, D., Müller, W., Oron, S., Renema, W., 2013. Eocene seasonality and seawater alkaline earth reconstruction using shallow-dwelling large benthic foraminifera. Earth Planet. Sci. Lett. 381, 104–115. https://doi.org/10.1016/j.epsl.2013.08.035.

Evans, D., Brugger, J., Inglis, G.N., Valdes, P., 2024. The temperature of the deep ocean is a robust proxy for global mean surface temperature during the Cenozoic. Paleoceanogr. Paleoclimatol. 39. https://doi.org/10.1029/2023PA004788 e2023PA004788.

Ffield, A., Vranes, K., Gordon, A.L., Dwi Susanto, R., Garzoli, S.L., 2000. Temperature variability within Makassar Strait. Geophys. Res. Lett. 27, 237–240. https://doi.org/10.1029/1999GL002377.

Fiebig, J., Bajnai, D., Löffler, N., Methner, K., Krsnik, E., Mulch, A., Hofmann, S., 2019. Combined high-precision $\Delta_{48}$ and $\Delta_{47}$ analysis of carbonates. Chem. Geol. 522, 186–191. https://doi.org/10.1016/j.chemgeo.2019.05.019.

Fiebig, J., Daëron, M., Bernecker, M., Guo, W., Schneider, G., Boch, R., Bernasconi, S.M., Jautzy, J., Dietzel, M., 2021. Calibration of the dual clumped isotope thermometer for carbonates. Geochim. Cosmochim. Acta. https://doi.org/10.1016/j.gca.2021.07.012.

Fiebig, J., Bernecker, M., Meijer, N., Methner, K., Staudigel, P.T., Davies, A.J., Bayarjargal, L., Spahr, D., Winkler, B., Hofmann, S., Granzin, M., Petersen, S.V., 2024. Carbonate clumped isotope values compromised by nitrate-derived NO2 interferent. Chem. Geol. 670, 122382. https://doi.org/10.1016/j.chemgeo.2024.122382.

Fietzke, J., Frische, M., 2016. Experimental evaluation of elemental behavior during LA-ICP-MS: influences of plasma conditions and limits of plasma robustness. J. Anal. At. Spectrom. 31, 234–244. https://doi.org/10.1039/C5JA00253B.

Fousiya, A.A., Malik, J.N., Paul, D., Chakraborty, S., Achyuthan, H., 2024. Microstructure and growth rate variability in a giant clam (*Tridacna maxima*) from the Lakshadweep Archipelago, India: implications for their use as biological monitors to trace extreme weather events. Coral Reefs. https://doi.org/10.1007/s00338-023-02455-8.

Fox, L.R., Wade, B.S., Holbourn, A., Leng, M.J., Bhatia, R., 2021. Temperature gradients across the Pacific Ocean during the middle Miocene. Paleoceanogr. Paleoclimatol. 36 (6) e2020PA003924.

Fröhlich, L., Siebert, V., Walliser, E.O., Thébault, J., Jochum, K.P., Chauvaud, L., Schöne, B.R., 2022. Ba/Ca profiles in shells of *Pecten maximus* – a proxy for specific primary producers rather than bulk phytoplankton. Chem. Geol. 593, 120743. https://doi.org/10.1016/j.chemgeo.2022.120743.

Gallagher, S.J., Auer, G., Brierley, C.M., Fulthorpe, C.S., Hall, R., 2024. Cenozoic history of the Indonesian Gateway. Annu. Rev. Earth Planet. Sci. 52, 581–604. https://doi.org/10.1146/annurev-earth-040722-111322.

Garbe-Schönberg, D., Müller, S., 2014. Nano-particulate pressed powder tablets for LA-ICP-MS. J. Anal. At. Spectrom. 29, 990–1000. https://doi.org/10.1039/C4JA00007B.

Gillikin, D.P., Lorrain, A., Navez, J., Taylor, J.W., André, L., Keppens, E., Baeyens, W., Dehairs, F., 2005. Strong biological controls on Sr/Ca ratios in aragonitic marine bivalve shells. Geochem. Geophys. Geosyst. 6. https://doi.org/10.1029/2004GC000874.

Gillikin, D.P., Lorrain, A., Paulet, Y.-M., André, L., Dehairs, F., 2008. Synchronous barium peaks in high-resolution profiles of calcite and aragonite marine bivalve shells. Geo-Mar. Lett. 28, 351–358. https://doi.org/10.1007/s00367-008-0111-9.

Griffiths, N., Müller, W., Johnson, K.G., Aguilera, O.A., 2013. Evaluation of the effect of diagenetic cements on element/Ca ratios in aragonitic early Miocene (~16Ma) Caribbean corals: implications for 'deep-time' palaeo-environmental reconstructions. Palaeogeogr. Palaeoclimatol. Palaeoecol. 369, 185–200. https://doi.org/10.1016/j.palaeo.2012.10.018.

Groeneveld, J., Henderiks, J., Renema, W., McHugh, C.M., De Vleeschouwer, D., Christensen, B.A., Fulthorpe, C.S., Reuning, L., Gallagher, S.J., Bogus, K., Auer, G., Ishiwa, T., Expedition 356 Scientists, 2017. Australian shelf sediments reveal shifts in Miocene Southern Hemisphere westerlies. Sci. Adv. 3, e1602567. https://doi.org/10.1126/sciadv.1602567.

Grossman, E.L., Ku, T.-L., 1986. Oxygen and carbon isotopic fractionation in biogenic aragonite: temperature effects. Chem. Geol. 59, 59–74. https://doi.org/10.1016/0168-9622(86)90057-6.

Harris, C.R., Millman, K.J., van der Walt, S.J., Gommers, R., Virtanen, P., Cournapeau, D., Wieser, E., Taylor, J., Berg, S., Smith, N.J., Kern, R., Picus, M., Hoyer, S., van Kerkwijk, M.H., Brett, M., Haldane, A., del Río, J.F., Wiebe, M., Peterson, P., Gérard-Marchant, P., Sheppard, K., Reddy, T., Weckesser, W., Abbasi, H., Gohlke, C., Oliphant, T.E., 2020. Array programming with NumPy. Nature 585, 357–362. https://doi.org/10.1038/s41586-020-2649-2.

Harzhauser, M., Mandic, O., Piller, W.E., Reuter, M., Kroh, A., 2008. Tracing back the origin of the indo-pacific mollusc fauna: basal tridacninae from the oligocene and miocene of the sultanate of Oman. Palaeontology 51, 199–213. https://doi.org/10.1111/j.1475-4983.2007.00742.x.

Holbourn, A., Kuhnt, W., Schulz, M., Erlenkeuser, H., 2005. Impacts of orbital forcing and atmospheric carbon dioxide on Miocene ice-sheet expansion. Nature 438, 483–487. https://doi.org/10.1038/nature04123.

Holbourn, A., Kuhnt, W., Regenberg, M., Schulz, M., Mix, A., Andersen, N., 2010. Does antarctic glaciation force migration of the tropical rain belt? Geology 38, 783–786. https://doi.org/10.1130/G31043.1.

Hori, M., Sano, Y., Ishida, A., Takahata, N., Shirai, K., Watanabe, T., 2015. Middle Holocene daily light cycle reconstructed from the strontium/calcium ratios of a fossil giant clam shell. Sci. Rep. 5, 8734. https://doi.org/10.1038/srep08734.

Ivany, L., Judd, E., 2022. Deciphering temperature seasonality in Earth's ancient oceans. Annu. Rev. Earth Planet. Sci. 50, 123–152. https://doi.org/10.1146/annurev-earth-032320-095156.

Ivany, L.C., Runnegar, B., 2010. Early Permian seasonality from bivalve $\delta^{18}O$ and implications for the oxygen isotopic composition of seawater. Geology 38, 1027–1030. https://doi.org/10.1130/G31330.1.

Jochum, K.P., Stoll, B., Herwig, K., Willbold, M., Hofmann, A.W., Amini, M., Aarburg, S., Abouchami, W., Hellebrand, E., Mocek, B., Raczek, I., Stracke, A., Alard, O., Bouman, C., Becker, S., Dücking, M., Brätz, H., Klemd, R., de Bruin, D., Canil, D., Cornell, D., de Hoog, C.-J., Dalpé, C., Danyushevsky, L., Eisenhauer, A., Gao, Y., Snow, J.E., Groschopf, N., Günther, D., Latkoczy, C., Guillong, M., Hauri, E.H., Höfer, H.E., Lahaye, Y., Horz, K., Jacob, D.E., Kasemann, S.A., Kent, A.J.R., Ludwig, T., Zack, T., Mason, P.R.D., Meixner, A., Rosner, M., Misawa, K., Nash, B.P., Pfänder, J., Premo, W.R., Sun, W.D., Tiepolo, M., Vannucci, R., Vennemann, T., Wayne, D., Woodhead, J.D., 2006. MPI-DING reference glasses for in situ microanalysis: new reference values for element concentrations and isotope ratios. Geochem. Geophys. Geosyst. 7, Q02008. https://doi.org/10.1029/2005GC001060.

Jochum, K.P., Weis, U., Stoll, B., Kuzmin, D., Yang, Q., Raczek, I., Jacob, D.E., Stracke, A., Birbaum, K., Frick, D.A., Günther, D., Enzweiler, J., 2011. Determination of Reference Values for NIST SRM 610–617 Glasses following ISO guidelines. Geostand. Geoanal. Res. 35, 397–429. https://doi.org/10.1111/j.1751-908X.2011.00120.x.

John, C.M., Karner, G.D., Browning, E., Leckie, R.M., Mateo, Z., Carson, B., Lowery, C., 2011. Timing and magnitude of Miocene eustasy derived from the mixed siliciclastic-carbonate stratigraphic record of the northeastern Australian margin. Earth Planet. Sci. Lett. 304, 455–467. https://doi.org/10.1016/j.epsl.2011.02.013.

Kim, S.-T., Mucci, A., Taylor, B.E., 2007. Phosphoric acid fractionation factors for calcite and aragonite between 25 and 75 °C: Revisited. Chem. Geol. 246, 135–146. https://doi.org/10.1016/j.chemgeo.2007.08.005.

Kniest, J.F., Davies, A.J., Brugger, J., Fiebig, J., Bernecker, M., Todd, J.A., Hickler, T., Voigt, S., Woodland, A., Raddatz, J., 2024. Dual clumped isotopes from Mid-Eocene bivalve shell reveal a hot and summer wet climate of the Paris Basin. Commun. Earth Environ. 5, 1–10. https://doi.org/10.1038/s43247-024-01491-8.

Knop, D., 1996. Giant Clams: A Comprehensive Guide to the Identification and Care of Tridacnid Clams. Dähne Verlag, Ettlingen.

Komagoe, T., Watanabe, T., Shirai, K., Yamazaki, A., Uematu, M., 2018. Geochemical and microstructural signals in Giant Clam *Tridacna maxima* Recorded Typhoon events at Okinotori Island. Japan. J. Geophys. Res. Biogeosci. 123, 1460–1474. https://doi.org/10.1029/2017JG004082.

Kuhnt, W., Holbourn, A., Hall, R., Zuvela, M., Käse, R., 2004. Neogene history of the Indonesian throughflow. In: Continent-Ocean Interactions within East Asian Marginal Seas. Am. Geophys. Union (AGU), pp. 299–320. https://doi.org/10.1029/149GM16.

LaRiviere, J.P., Ravelo, A.C., Crimmins, A., Dekens, P.S., Ford, H.L., Lyle, M., Wara, M. W., 2012. Late Miocene decoupling of oceanic warmth and atmospheric carbon dioxide forcing. Nature 486, 97–100. https://doi.org/10.1038/nature11200.

Lear, C.H., Elderfield, H., Wilson, P.A., 2000. Cenozoic deep-sea temperatures and global ice volumes from Mg/Ca in benthic foraminiferal calcite. Science 287, 269–272. https://doi.org/10.1126/science.287.5451.269.

Li, M., Hinnov, L., Kump, L., 2019. *Acycle*: time-series analysis software for paleoclimate research and education. Comput. Geosci. 127, 12–22. https://doi.org/10.1016/j.cageo.2019.02.011.

Longerich, H.P., Jackson, S.E., Günther, D., 1996. Inter-laboratory note. Laser ablation inductively coupled plasma mass spectrometric transient signal data acquisition and analyte concentration calculation. J. Anal. At. Spectrom. 11, 899–904. https://doi.org/10.1039/JA9961100899.

Ma, X., Yan, H., Fei, H., Liu, C., Shi, G., Huang, E., Wang, Y., Qu, X., Lian, E., Dang, H., 2020. A high-resolution $\delta^{18}O$ record of modern *Tridacna gigas* bivalve and its paleoenvironmental implications. Palaeogeogr. Palaeoclimatol. Palaeoecol. 554, 109800. https://doi.org/10.1016/j.palaeo.2020.109800.

Marali, S., Schöne, B.R., Mertz-Kraus, R., Griffin, S.M., Wanamaker, A.D., Butler, P.G., Holland, H.A., Jochum, K.P., 2017. Reproducibility of trace element time-series (Na/Ca, Mg/Ca, Mn/Ca, Sr/Ca, and Ba/Ca) within and between specimens of the bivalve *Arctica islandica* – a LA-ICP-MS line scan study. Palaeogeogr. Palaeoclimatol. Palaeoecol. 484, 109–128. https://doi.org/10.1016/j.palaeo.2016.11.024.

McArthur, J.M., Howarth, R.J., 2005. Strontium isotope stratigraphy. In: Smith, A.G., Gradstein, F.M., Ogg, J.G. (Eds.), A Geologic Time Scale 2004. Cambridge University Press, Cambridge, pp. 96–105. https://doi.org/10.1017/CBO9780511536045.008.

McArthur, J.M., Howarth, R.J., Bailey, T.R., 2001. Strontium isotope stratigraphy: LOWESS version 3: best fit to the marine Sr-isotope curve for 0–509 Ma and accompanying look-up table for deriving numerical age. J. Geol. 109, 155–170. https://doi.org/10.1086/319243.

McPhaden, M.J., Lee, T., Fournier, S., Balmaseda, M.A., 2020. ENSO observations. In: El Niño Southern Oscillation in a Changing Climate. Am. Geophys. Union (AGU), pp. 39–63. https://doi.org/10.1002/9781119548164.ch3.

Mei, Y., Shao, D., Wang, Y., Yang, Z., Yang, W.Q., Gao, Y., He, S., Zheng, Y., Li, A., Sun, L., 2018. Measurement of Sr/Ca ratio in tridacna spp. Shells from South China Sea: a comparison of SR-XRF and ICP-OES analysis methods. Spectrosc. Spectr. Anal. 38, 1640–1647. https://doi.org/10.3964/j.issn.1000-0593(2018)05-1640-08.

Mills, K., John, E.H., Muir, D.D., Santodomingo, N., Johnson, K.G., Hussein, M.A.S., Sosdian, S., 2023. Growth responses of mixotrophic giant clams on nearshore turbid coral reefs. Coral Reefs 42, 593–608. https://doi.org/10.1007/s00338-023-02366-8.

Moon, L.R., Judd, E.J., Thomas, J., Ivany, L.C., 2021. Out of the oven and into the fire: unexpected preservation of the seasonal $\delta^{18}O$ cycle following heating experiments on shell carbonate. Palaeogeogr. Palaeoclimatol. Palaeoecol. 562, 110115. https://doi.org/10.1016/j.palaeo.2020.110115.

Müller, W., Shelley, M., Miller, P., Broude, S., 2009. Initial performance metrics of a new custom-designed ArF excimer LA-ICPMS system coupled to a two-volume laser-ablation cell. J. Anal. At. Spectrom. 24, 209–214. https://doi.org/10.1039/B805995K.

Nathan, S.A., Leckie, R.M., 2009. Early history of the Western Pacific warm pool during the middle to late Miocene (~13.2–5.8 Ma): role of sea-level change and implications for equatorial circulation. Palaeogeogr. Palaeoclimatol. Palaeoecol. 274, 140–159.

Nützel, A., Joachimski, M., Correa, M.L., 2010. Seasonal climatic fluctuations in the late Triassic tropics—High-resolution oxygen isotope records from aragonitic bivalve shells (Cassian Formation, Northern Italy). Palaeogeogr. Palaeoclimatol. Palaeoecol. 285, 194–204. https://doi.org/10.1016/j.palaeo.2009.11.011.

Paton, C., Hellstrom, J., Paul, B., Woodhead, J., Hergt, J., 2011. Iolite: Freeware for the visualisation and processing of mass spectrometric data. J. Anal. At. Spectrom. 26, 2508–2518. https://doi.org/10.1039/C1JA10172B.

Pätzold, J., Heinrichs, J.P., Wolschendorf, K., Wefer, G., 1991. Correlation of stable oxygen isotope temperature record with light attenuation profiles in reef-dwelling *Tridacna* shells. Coral Reefs 10, 65–69. https://doi.org/10.1007/BF00571825.

Peharda, M., Schöne, B.R., Black, B.A., Corrège, T., 2021. Advances of sclerochronology research in the last decade. Palaeogeogr. Palaeoclimatol. Palaeoecol. 570, 110371. https://doi.org/10.1016/j.palaeo.2021.110371.

Pound, M.J., Haywood, A.M., Salzmann, U., Riding, J.B., Lunt, D.J., Hunter, S.J., 2011. A Tortonian (late Miocene, 11.61–7.25Ma) global vegetation reconstruction. Palaeogeogr. Palaeoclimatol. Palaeoecol. 300, 29–45. https://doi.org/10.1016/j.palaeo.2010.11.029.

Purwandari, R.N., Mubarrok, S., Mandang, I., 2019. Sea surface temperature variability in the Makassar strait during ENSO (El niño Southern Oscillation) from the Terra-MODIS data sets. J. Phys. Conf. Ser. 1282, 012052. https://doi.org/10.1088/1742-6596/1282/1/012052.

Rae, J.W.B., Zhang, Y.G., Liu, X., Foster, G.L., Stoll, H.M., Whiteford, R.D.M., 2021. Atmospheric $CO_2$ over the past 66 Million Years from Marine Archives. Annu. Rev. Earth Planet. Sci. 49, 609–641. https://doi.org/10.1146/annurev-earth-082420-063026.

Reback, J., McKinney, W., den Bossche, J.V., Roeschke, M., Augspurger, T., Hawkins, S., Cloud, P., Hoefler, P., Klein, A., Petersen, T., Tratner, J., She, C., Ayd, W., Naveh, S., Darbyshire, J.H.M., Shadrach, R., Garcia, M., Schendel, J., Hayden, A., Saxton, D., Gorelli, M.E., Li, F., Wörtwein, T., Zeitlin, M., Jancauskas, V., McMaster, A., Li, T., 2022. Pandas-Dev/Pandas: Pandas 1.4.3. https://doi.org/10.5281/zenodo.6702671.

Renema, W., Warter, V., Novak, V., Young, J.R., Marshall, N., Hasibuan, F., 2015. Ages of Miocene fossil localities in the northern Kutai Basin (East Kalimantan, Indonesia). PALAIOS 30, 26–39. https://doi.org/10.2110/palo.2013.127.

Rohling, E.J., Foster, G.L., Gernon, T.M., Grant, K.M., Heslop, D., Hibbert, F.D., Roberts, A.P., Yu, J., 2022. Comparison and synthesis of sea-level and deep-sea temperature variations over the past 40 million years. Rev. Geophys. 60. https://doi.org/10.1029/2022RG000775 e2022RG000775.

Rosewater, J., 1965. The family tridacnidae in the Indo-Pacific. Indo-Pac. Mollusca 1, 153.

Rossbach, S., Saderne, V., Anton, A., Duarte, C.M., 2019. Light-dependent calcification in Red Sea giant clam Tridacna maxima. Biogeosciences 16, 2635–2650. https://doi.org/10.5194/bg-16-2635-2019.

Russell, W.A., Papanastassiou, D.A., Tombrello, T.A., 1978. Ca isotope fractionation on the Earth and other solar system materials. Geochim. Cosmochim. Acta 42, 1075–1090. https://doi.org/10.1016/0016-7037(78)90105-9.

Sano, Y., Kobayashi, S., Shirai, K., Takahata, N., Matsumoto, K., Watanabe, T., Sowa, K., Iwai, K., 2012. Past daily light cycle recorded in the strontium/calcium ratios of giant clam shells. Nat. Commun. 3, 761. https://doi.org/10.1038/ncomms1763.

Sano, Y., Okumura, T., Murakami-Sugihara, N., Tanaka, K., Kagoshima, T., Ishida, A., Hori, M., Snyder, G.T., Takahata, N., Shirai, K., 2021. Influence of normal tide and the Great Tsunami as recorded through hourly-resolution micro-analysis of a mussel shell. Sci. Rep. 11, 19874. https://doi.org/10.1038/s41598-021-99361-2.

Schleinkofer, N., Raddatz, J., Evans, D., Gerdes, A., Flögel, S., Voigt, S., Büscher, J.V., Wisshak, M., 2021. Compositional variability of Mg/Ca, Sr/Ca, and Na/Ca in the deep-sea bivalve *Acesta excavata* (Fabricius, 1779). PLoS One 16, e0245605. https://doi.org/10.1371/journal.pone.0245605.

Schmidt, G.A., Annan, J.D., Bartlein, P.J., Cook, B.I., Guilyardi, E., Hargreaves, J.C., Harrison, S.P., Kageyama, M., LeGrande, A.N., Konecky, B., Lovejoy, S., Mann, M.E., Masson-Delmotte, V., Risi, C., Thompson, D., Timmermann, A., Tremblay, L.-B., Yiou, P., 2014. Using palaeo-climate comparisons to constrain future projections in CMIP5. Clim. Past 10, 221–250. https://doi.org/10.5194/cp-10-221-2014.

Schneider, N., 1998. The Indonesian throughflow and the Global climate system. J. Clim. 11, 676–689. https://doi.org/10.1175/1520-0442(1998)011<0676:TITATG>2.0.CO;2.

Schöne, B.R., Radermacher, P., Zhang, Z., Jacob, D.E., 2013. Crystal fabrics and element impurities (Sr/Ca, Mg/Ca, and Ba/Ca) in shells of Arctica islandica—Implications for paleoclimate reconstructions. Palaeogeography, Palaeoclimatology, Palaeoecology, Unraveling environmental histories from skeletal diaries -. advances in sclerochronology 373, 50–59. https://doi.org/10.1016/j.palaeo.2011.05.013.

Schöne, B.R., Zhang, Z., Jacob, D., Gillikin, D.P., Tütken, T., Garbe-Schönberg, D., Mcconnaughey, T., Soldati, A., 2010. Effect of organic matrices on the determination of the trace element chemistry (Mg, Sr, Mg/Ca, Sr/Ca) of aragonitic bivalve shells (*Arctica islandica*)—Comparison of ICP-OES and LA-ICP-MS data. Geochem. J. 44, 23–37. https://doi.org/10.2343/geochemj.1.0045.

Schöne, B.R., Zhang, Z., Radermacher, P., Thébault, J., Jacob, D.E., Nunn, E.V., Maurer, A.-F., 2011. Sr/Ca and Mg/Ca ratios of ontogenetically old, long-lived bivalve shells (*Arctica islandica*) and their function as paleotemperature proxies. Palaeogeogr. Palaeoclimatol. Palaeoecol. 302, 52–64. https://doi.org/10.1016/j.palaeo.2010.03.016.

Schöne, B.R., Marali, S., Jantschke, A., Mertz-Kraus, R., Butler, P.G., Fröhlich, L., 2023. Can element chemical impurities in aragonitic shells of marine bivalves serve as proxies for environmental variability? Chem. Geol. 616, 121215. https://doi.org/10.1016/j.chemgeo.2022.121215.

Schwartzmann, C., Durrieu, G., Sow, M., Ciret, P., Lazareth, C.E., Massabuau, J.-C., 2011. In situ giant clam growth rate behavior in relation to temperature: a one-year coupled study of high-frequency noninvasive valvometry and sclerochronology. Limnol. Oceanogr. 56, 1940–1951. https://doi.org/10.4319/lo.2011.56.5.1940.

Shao, D., Mei, Y., Yang, Z., Wang, Y., Yang, W., Gao, Y., Yang, L., Sun, L., 2020. Holocene ENSO variability in the South China Sea recorded by high-resolution oxygen isotope records from the shells of *Tridacna spp*. Sci. Rep. 10, 3921. https://doi.org/10.1038/s41598-020-61013-2.

Sosdian, S.M., Lear, C.H., 2020. Initiation of the western Pacific warm pool at the middle Miocene climate transition? Paleoceanogr. Paleoclimatol. 35 (12) e2020PA003920.

Spötl, C., Vennemann, T.W., 2003. Continuous-flow isotope ratio mass spectrometric analysis of carbonate minerals. Rapid Commun. Mass Spectrom. 17, 1004–1006. https://doi.org/10.1002/rcm.1010.

Staudigel, P.T., Swart, P.K., 2016. Isotopic behavior during the aragonite-calcite transition: Implications for sample preparation and proxy interpretation. Chem. Geol. 442, 130–138. https://doi.org/10.1016/j.chemgeo.2016.09.013.

Staudigel, P., Davies, A.J., Bernecker, M., Tagliavento, M., Van Der Lubbe, H.J.L., Nooitgedacht, C., Looser, N., Bernasconi, S.M., Vonhof, H., Fiebig, J., 2023a. Fingerprinting kinetic isotope effects and diagenetic exchange reactions using fluid inclusion and dual-clumped isotope analysis. Geochem. Geophys. Geosyst. 24. https://doi.org/10.1029/2022GC010766 e2022GC010766.

Staudigel, P., Pederson, C., van der Lubbe, J., Bernecker, M., Tagliavento, M., Davies, A., Immenhauser, A., Fiebig, J., 2023b. An isotopologue-enabled model ($\Delta_{47}$, $\Delta_{48}$) for describing thermal Fluid-Carbonate interaction in open and closed diagenetic systems. Geochem. Geophys. Geosyst. 24. https://doi.org/10.1029/2023GC011117 e2023GC011117.

Steiger, R.H., Jäger, E., 1977. Subcommission on geochronology: convention on the use of decay constants in geo- and cosmochronology. Earth Planet. Sci. Lett. 36, 359–362. https://doi.org/10.1016/0012-821X(77)90060-7.

Steuber, T., Rauch, M., Masse, J.-P., Graaf, J., Malkoč, M., 2005. Low-latitude seasonality of cretaceous temperatures in warm and cold episodes. Nature 437, 1341–1344. https://doi.org/10.1038/nature04096.

Teichberg, M., Wild, C., Bednarz, V.N., Kegler, H.F., Lukman, M., Gärdes, A.A., Heiden, J. P., Weiand, L., Abu, N., Nasir, A., Miñarro, S., Ferse, S.C.A., Reuter, H., Plass-Johnson, J.G., 2018. Spatio-Temporal patterns in coral reef communities of the spermonde archipelago, 2012–2014, I: comprehensive reef monitoring of water and benthic indicators reflect changes in reef health. Front. Mar. Sci. 5, 33. https://doi.org/10.3389/fmars.2018.00033.

Tierney, J.E., Poulsen, C.J., Montañez, I.P., Bhattacharya, T., Feng, R., Ford, H.L., Hönisch, B., Inglis, G.N., Petersen, S.V., Sagoo, N., Tabor, C.R., Thirumalai, K., Zhu, J., Burls, N.J., Foster, G.L., Goddéris, Y., Huber, B.T., Ivany, L.C., Turner, S.K., Lunt, D.J., McElwain, J.C., Mills, B.J.W., Otto-Bliesner, B.L., Ridgwell, A., Zhang, Y. G., 2020. Past climates inform our future. Science 370. https://doi.org/10.1126/science.aay3701 eaay3701.

Timmermann, A., An, S.I., Kug, J.S., Jin, F.F., Cai, W., et al., 2018. El Niño–southern oscillation complexity. Nature 559, 535–545.

Torrence, C., Compo, G.P., 1998. A practical guide to wavelet analysis. Bull. Am. Meteorol. Soc. 79, 61–78. https://doi.org/10.1175/1520-0477(1998)079<0061:APGTWA>2.0.CO;2.

Veeh, H.H., Chappell, J., 1970. Astronomical theory of climatic change: support from New Guinea. Science 167, 862–865. https://doi.org/10.1126/science.167.3919.862.

Waite, A.J., Swart, P.K., 2015. The inversion of aragonite to calcite during the sampling of skeletal archives: implications for proxy interpretation. Rapid Commun. Mass Spectrom. 29, 955–964. https://doi.org/10.1002/rcm.7180.

Walliser, E.O., Mertz-Kraus, R., Schöne, B.R., 2018. The giant inoceramid *Platyceramus platinus* as a high-resolution paleoclimate archive for the late cretaceous of the Western Interior Seaway. Cretac. Res. 86, 73–90. https://doi.org/10.1016/j.cretres.2018.01.010.

Warter, V., Müller, W., 2017. Daily growth and tidal rhythms in Miocene and modern giant clams revealed via ultra-high resolution LA-ICPMS analysis — a novel methodological approach towards improved sclerochemistry. Palaeogeogr. Palaeoclimatol. Palaeoecol. 465, 362–375. https://doi.org/10.1016/j.palaeo.2016.03.019.

Warter, V., Müller, W., Wesselingh, F.P., Todd, J.A., Renema, W., 2015. Late Miocene seasonal to subdecadal climate variability in the Indo-West Pacific (East Kalimantan, Indonesia) preserved in giant clams. PALAIOS 30, 66–82. https://doi.org/10.2110/palo.2013.061.

Warter, V., Erez, J., Müller, W., 2018. Environmental and physiological controls on daily trace element incorporation in *Tridacna crocea* from combined laboratory culturing and ultra-high resolution LA-ICP-MS analysis. Palaeogeogr. Palaeoclimatol. Palaeoecol. 496, 32–47. https://doi.org/10.1016/j.palaeo.2017.12.038.

Watanabe, T., Suzuki, A., Kawahata, H., Kan, H., Ogawa, S., 2004. A 60-year isotopic record from a mid-Holocene fossil giant clam (*Tridacna gigas*) in the Ryukyu Islands: physiological and paleoclimatic implications. Palaeogeogr. Palaeoclimatol. Palaeoecol. 212, 343–354. https://doi.org/10.1016/j.palaeo.2004.07.001.

Welsh, K., Elliot, M., Tudhope, A., Ayling, B., Chappell, J., 2011. Giant bivalves (*Tridacna gigas*) as recorders of ENSO variability. Earth Planet. Sci. Lett. 307, 266–270. https://doi.org/10.1016/j.epsl.2011.05.032.

Yamanaka, M.D., Ogino, S.-Y., Wu, P.-M., Jun-Ichi, H., Mori, S., Matsumoto, J., Syamsudin, F., 2018. Maritime continent coastlines controlling Earth's climate. Prog. Earth Planet Sci. 5, 21. https://doi.org/10.1186/s40645-018-0174-9.

Yan, H., 2020. Daily growth bands of giant clam shell: a potential paleoweather recorder. Solid Earth Sci. 5, 249–253. https://doi.org/10.1016/j.sesci.2020.10.001.

Yan, H., Shao, D., Wang, Y., Sun, L., 2013. Sr/Ca profile of long-lived *Tridacna gigas* bivalves from South China Sea: a new high-resolution SST proxy. Geochim. Cosmochim. Acta 112, 52–65. https://doi.org/10.1016/j.gca.2013.03.007.

Yuan, S., Chiang, H.-W., Liu, G., Bijaksana, S., He, S., Jiang, X., Imran, A.M., Wicaksono, S.A., Wang, X., 2023. The strength, position, and width changes of the intertropical convergence zone since the Last Glacial Maximum. Proc. Natl. Acad. Sci. 120. https://doi.org/10.1073/pnas.2217064120 e2217064120.

Zhang, Y.G., Pagani, M., Liu, Z., 2014. A 12-million-year temperature history of the tropical Pacific Ocean. Science 344, 84–87. https://doi.org/10.1126/science.1246172.

Zhang, T., Yang, S., Jiang, X., Zhao, P., 2016. Seasonal–interannual variation and prediction of wet and dry season rainfall over the maritime continent: roles of ENSO

and monsoon circulation. J. Clim. 29, 3675–3695. https://doi.org/10.1175/JCLI-D-15-0222.1.